

# Evaluating the stretching/compression effect of Richtmyer–Meshkov instability in convergent geometries

Jin Ge<sup>1</sup>, Haifeng Li<sup>2,†</sup>, Xinting Zhang<sup>1</sup> and Baolin Tian<sup>2,3,†</sup>

<sup>1</sup>Sino-French Engineer School, Beihang University, Beijing 100191, PR China

<sup>2</sup>Institute of Applied Physics and Computational Mathematics, Beijing 100094, PR China

<sup>3</sup>HEDPS, Center for Applied Physics and Technology, and College of Engineering, Peking University, Beijing 100871, PR China

(Received 9 December 2021; revised 10 May 2022; accepted 30 June 2022)

Richtmyer–Meshkov (RM) instability in convergent geometries (such as cylinders and spheres) plays a fundamental role in natural phenomena and engineering applications, e.g. supernova explosion and inertial confinement fusion. Convergent geometry refers to a system in which the interface converges and the fluids are compressed correspondingly. By applying a decomposition formula, the stretching or compression (S(C)) effect is separated from the perturbation growth as one of the main contributions, which is defined as the averaged velocity difference between two ends of the mixing zone. Starting from linear theories, the S(C) effect in planar, cylindrical and spherical geometries is derived as a function of geometrical convergence ratio, compression ratio and mixing width. Specifically, geometrical convergence stretches the mixing zone, while fluid compression compresses the mixing zone. Moreover, the contribution of geometrical convergence in the spherical geometry is more important than that in the cylindrical geometry. A series of cylindrical cases with high convergence ratio is simulated, and the growth of perturbations is compared with that of the corresponding planar cases. As a result, the theoretical results of the S(C) effect agree well with the numerical results. Furthermore, results show that the S(C) effect is a significant feature in convergent geometries. Therefore, the S(C) effect is an important part of the Bell–Plesset effect. The present work on the S(C) effect is important for further modelling of the mixing width of convergent RM instabilities.

**Key words:** nonlinear instability, buoyancy-driven instability

† Email addresses for correspondence: [tylihaifeng@163.com](mailto:tylihaifeng@163.com), [tian\\_baolin@iapcm.ac.cn](mailto:tian_baolin@iapcm.ac.cn)

## 1. Introduction

Perturbations existing on a material interface grow after being accelerated by an incident shock wave or by an external force directed from the heavy fluid to the light fluid, which are known as Richtmyer–Meshkov (RM) instability (Richtmyer 1960; Meshkov 1969) and Rayleigh–Taylor (RT) instability (Rayleigh 1882; Taylor 1950), respectively. The pressure gradient caused by the shock wave or the external force does not coincide with the density gradient, which produces a baroclinic source term depositing vorticity around the material interface. The interface is thus rolled up, forming bubbles where the light fluid penetrates into the heavy fluid, and spikes where the heavy fluid penetrates into the light fluid. At late time, the nonlinear effect causes the interfacial instability to transition into turbulent mixing. The evolution of mixing width ( $W$ ), defined as the distance from the bubble front to the spike front, has been investigated extensively, which is reviewed systematically in a series of papers (Brouillette 2002; Zhou 2017*a,b*; Zhai *et al.* 2018; Zhou *et al.* 2021).

The classical RM instability, which occurs at a planar interface, has been investigated widely. However, in many engineering applications, such as inertial confinement fusion (Thomas & Kares 2012; Betti & Hurricane 2016), the interface is always a collapsing cylinder or sphere. These interface configurations are referred to collectively as convergent geometries. Built on the understanding of planar RM instability, researches have been carried out on convergent RM instability. Early-time linear (Bell 1951; Plesset 1954) and weakly nonlinear (Wang *et al.* 2015; Zhang *et al.* 2020) growth of the single-mode perturbation in the convergent geometry are described mathematically. These models have been confirmed by a series of experiments (Ding *et al.* 2017; Luo *et al.* 2018*b*, 2019). Theoretical analyses were extended in recent studies to predict the growth of perturbations in the case of multiple shocks (Flaig *et al.* 2018), nonlinear stages (Goncharov & Li 2005; Zhao *et al.* 2020; Dimonte 2021), or late-time turbulent mixing (Mikaelian 1990, 2005; Rafei *et al.* 2019; El Rafei & Thornber 2020). Besides, numerical simulations have been carried out to investigate the convergent RM instability. Joggerst *et al.* (2014) presented two-dimensional spherical and cylindrical implosion cases with different grids, and showed that the results obtained from different grids converge under high resolution. Lombardini, Pullin & Meiron (2014*a,b*) simulated numerically the RM instability with multi-mode perturbations in spherical geometry, and divided the growth of the mixing width into three parts based on a linear theory: RT-like contribution, geometric convergence, and compression effects. A series of cylindrical implosion experiments were carried out (Hsing & Hoffman 1997; Hsing *et al.* 1997; Tubbs *et al.* 1999; Barnes *et al.* 2002; Lanier *et al.* 2003). In the experiments, the smooth premixing layer is observed to be thickened during convergence (Lanier *et al.* 2003), which has not been understood clearly.

One key problem is how to evaluate the difference between the growth of perturbations in convergent geometries and that in the planar geometry. Bell (1951) and Plesset (1954) extended the single-mode linear theory to the cylindrical and spherical geometry, respectively, which are summarized by Epstein (2004) as

$$\left(\gamma_\rho + \frac{d}{dt}\right) \frac{d}{dt}(\rho a) = \gamma_0^2(\rho a), \quad (1.1a)$$

$$\left(\gamma_\rho + \frac{d}{dt}\right) \frac{d}{dt}(\rho a R) = \gamma_0^2(\rho a R) \quad (1.1b)$$

and

$$\left(\gamma_R + \gamma_\rho + \frac{d}{dt}\right) \frac{d}{dt}(\rho a R^2) = \gamma_0^2(\rho a R^2) \quad (1.1c)$$

for planar, cylindrical and spherical geometries, respectively. Here,  $\gamma_R = -\dot{R}/R$  is the convergence rate of the interface, and  $\gamma_\rho = -\dot{\rho}/\rho$  is the compression rate of the fluids. The overdot represents the time derivative. Also,  $a$  is the perturbation amplitude, and  $\gamma_0$  is the growth rate, where

$$\gamma_0^2 = \frac{2\pi m}{L} \frac{\rho_h - \rho_l}{\rho_h + \rho_l} g \quad (1.2a)$$

for the planar geometry,

$$\gamma_0^2 = \frac{m}{R} \frac{\rho_h - \rho_l}{\rho_h + \rho_l} g \quad (1.2b)$$

for the cylindrical geometry, and

$$\gamma_0^2 = \frac{m(m+1)}{R} \frac{\rho_h - \rho_l}{m\rho_h + (m+1)\rho_l} g \quad (1.2c)$$

for the spherical geometry. Here,  $\rho_h$  and  $\rho_l$  are the densities of heavy fluid and light fluid,  $L$  is the length of the cross-section in the planar geometry, which is a constant,  $R$  is the interface radius, which varies with time,  $m$  is the wavenumber of the perturbations, and  $g$  is the acceleration of the interface. Compared with the planar cases, the linear theory in convergent geometry is characterized with  $R$ , which varies with time, and  $\dot{\rho}$ , which represents the variation of density with time. In the weakly nonlinear model deduced by Wang *et al.* (2015) and Zhang *et al.* (2020), geometrical convergence is also verified as an important factor to modify the growth of perturbation. The perturbation growth is found to be amplified in the convergent geometries, which is described as a function of the convergence ratio  $C_r = R_0/R(t)$ . For example, by assuming a self-similar growth of perturbation, Mikaelian (1990, 2005) extended the linear theory to predict the growth of the turbulent-mixing width in both cylindrical and spherical geometries, where the convergence ratio  $C_r$  also amplifies the growth of the mixing width. Therefore, compared to that in the planar geometry, the perturbation growth in the convergent geometry is modified. This modification caused by the geometry is referred to collectively as the Bell–Plesset (BP) effect (Beck 1996; Hsing & Hoffman 1997), which is a function of  $R$  and  $\rho$ . As suggested in the inertial confinement fusion experiments by Li *et al.* (2004), the BP effect is expected to become important at a much higher convergence ratio  $C_r > 30$ .

The BP effect is caused mainly by geometrical convergence and fluid compression. However, the relative importance and coupling of the two factors are unclear. On the one hand, by assuming a constant mass in the mixing zone with constant density, the stretching of the mixing width  $W$  (the radial length) is deduced since the azimuthal length of the mixing zone decreases as the interface converges (Luo *et al.* 2018a). On the other hand, supposing that the fluids are compressed uniformly in space, the coupling effect of geometrical convergence and fluid compression turns out to inhibit the growth of perturbations (Epstein 2004), which leads to a different conclusion. More recently, Ge *et al.* (2020) carried out three-dimensional simulations of cylindrical RM instability. As a result, a stretching effect exists obviously in cylindrical geometry. The stretching effect is defined as the averaged velocity difference between two ends of the mixing zone (Li *et al.* 2021), which does not exist in planar geometry if there is no wave acting on the mixing zone. Ge *et al.* (2020) ascribe this stretching effect in cylindrical geometry to ‘an asymmetric geometric environment’. However, there is no detailed explanation of this asymmetric geometric environment. Furthermore, the relation between this stretching effect and the BP effect is still unclear. Therefore, to better understand the BP effect,

it is worthwhile to give the exact quantitative contribution of geometrical convergence and fluid compression in the modification caused by the convergent geometry. Besides, an intuitive physical explanation of this modification on the perturbation growth in convergent geometries is also needed, which motivates the present work.

In this work, we extract a compression or stretching (S(C)) effect from the perturbation growth. We evaluate quantitatively the S(C) effect, and prove this effect to be an important part of the BP effect. The physical origin underlying the S(C) effect is also given. A series of numerical simulations in planar and cylindrical geometries are performed to verify our theoretical analysis.

The layout of this paper is as follows. The theoretical analysis is presented in § 2, where the S(C) effect is introduced and analysed. In § 3, the physical model and numerical method for numerical simulations are presented. The numerical results can be found in § 4, followed by the discussion about the S(C) effect in § 5. The conclusions are drawn in § 6. The reliability of the numerical simulations is discussed in [Appendices A and B](#).

## 2. Theoretical analysis on the S(C) effect

### 2.1. Definition of the S(C) effect

The definition of the S(C) effect is given by applying a decomposition formula. The formula was proposed to investigate the influence of nonlinear waves (Li *et al.* 2021) and convergent geometry (Ge *et al.* 2020) on the evolution of RM instability. For completeness, we give a brief derivation of the S(C) effect.

The mixing width is defined as the distance from the bubble-zone front to the spike-zone front, i.e.

$$W \equiv \text{sgn}(A) (R_B - R_S), \tag{2.1a}$$

and hence

$$\dot{W} = \text{sgn}(A) (\dot{R}_B - \dot{R}_S), \tag{2.1b}$$

where the overdot means the time derivative,  $A = (\rho_{out} - \rho_{in})/(\rho_{out} + \rho_{in})$  is the Atwood number,  $R_B$  is the radius where the Favre-averaged light-fluid mass fraction profile in the streamwise direction  $\tilde{Y}_l(R_B, t) = 0.01$ , and  $R_S$  is the radius where  $\tilde{Y}_l(R_S, t) = 0.99$ .

For a physical variable  $f, \bar{f}$  and  $\tilde{f}$  represent the Reynolds-averaged streamwise-direction profile and the Favre-averaged streamwise-direction profile, respectively. Here,  $\tilde{f} = \bar{\rho}f/\bar{\rho}$ , where  $\rho$  is the fluid density. Correspondingly,  $f' = f - \bar{f}$  and  $f'' = f - \tilde{f}$  are the fluctuating parts of the variable. The averaged velocity is aligned in the streamwise direction. For consistency, in the planar geometry, we use  $r$  to indicate the streamwise direction.

For the Favre-averaged mass fraction profile  $\tilde{Y}(r, t)$ , where  $r$  is the streamwise direction, at any given time  $t$ , the function of space  $\tilde{Y}(r, t)$  is monotonic when  $\tilde{Y} \in (0, 1)$ . Therefore, the inverse function of  $\tilde{Y}(r, t)$  can be defined as  $R_{\tilde{Y}}(Y, t) = \tilde{Y}^{-1}(r, t)$  ( $Y \in (0, 1)$ ), where  $R_{\tilde{Y}}(Y, t)$  is the radius with an averaged mass fraction  $Y$  at time  $t$ . The time derivative of the radius with a certain mass fraction  $Y_0$  is formulated as

$$\dot{R}|_{Y_0} = \left. \frac{\partial R_{\tilde{Y}}}{\partial t} \right|_{Y_0} = \lim_{\Delta t \rightarrow 0} \frac{R_{\tilde{Y}}(Y_0, t + \Delta t) - R_{\tilde{Y}}(Y_0, t)}{\Delta t}. \tag{2.2}$$

For  $r_0 = R_{\tilde{Y}}(Y_0, t + \Delta t)$ , it is obvious that at time  $t$ , the radius  $r_0$  corresponds to another value of mass fraction  $Y_0 + \Delta Y$ , such that

$$r_0 = R_{\tilde{Y}}(Y_0, t + \Delta t) = R_{\tilde{Y}}(Y_0 + \Delta Y, t), \quad (2.3a)$$

$$-\Delta Y = \tilde{Y}(r_0, t + \Delta t) - \tilde{Y}(r_0, t). \quad (2.3b)$$

Substituting (2.3) into (2.2), we have

$$\left. \frac{\partial R_{\tilde{Y}}}{\partial t} \right|_{Y_0} = \lim_{\Delta t \rightarrow 0} \frac{R_{\tilde{Y}}(Y_0 + \Delta Y, t) - R_{\tilde{Y}}(Y_0, t)}{\Delta Y} \frac{\Delta Y}{\Delta t} = - \left. \frac{\partial R_{\tilde{Y}}}{\partial Y} \frac{\partial \tilde{Y}}{\partial t} \right|_{Y_0}. \quad (2.4)$$

The property of the inverse function indicates that  $\partial R_{\tilde{Y}}/\partial Y = (\partial \tilde{Y}/\partial r)^{-1}$ . Therefore, the velocity of the radius with a certain mass fraction  $Y_0$  can be expressed as

$$\dot{R}|_{Y_0} = - \left. \frac{\partial \tilde{Y}/\partial t}{\partial \tilde{Y}/\partial r} \right|_{Y_0}. \quad (2.5)$$

The governing equation of the mass fraction is

$$\frac{\partial \rho Y}{\partial t} + \nabla \cdot (\rho Y \mathbf{u}) = \nabla \cdot (\rho D \nabla Y), \quad (2.6)$$

where  $D$  is the diffusion coefficient. The Reynolds-averaged equation (2.6) is

$$\frac{\partial \bar{\rho} \tilde{Y}}{\partial t} + \nabla \cdot (\bar{\rho} \tilde{Y} \tilde{\mathbf{u}}) + \nabla \cdot \overline{\rho Y'' \mathbf{u}''} = \nabla \cdot (\bar{\rho} D \nabla \tilde{Y} + \overline{\rho D \nabla Y''}). \quad (2.7)$$

We now consider the averaged mass equation

$$\frac{\partial \bar{\rho}}{\partial t} + \nabla \cdot (\bar{\rho} \tilde{\mathbf{u}}) = 0. \quad (2.8)$$

Subtracting  $\tilde{Y}$  times (2.8) from (2.7), we obtain

$$\frac{\partial \tilde{Y}}{\partial t} + (\tilde{\mathbf{u}} \cdot \nabla) \tilde{Y} + \frac{1}{\bar{\rho}} \nabla \cdot \overline{\rho Y'' \mathbf{u}''} = \frac{1}{\bar{\rho}} \nabla \cdot (\bar{\rho} D \nabla \tilde{Y} + \overline{\rho D \nabla Y''}). \quad (2.9)$$

The spatial gradient in the streamwise direction has the same form for the Cartesian, cylindrical and spherical coordinates. Therefore, we use  $\nabla f = \mathbf{e}_r \partial f/\partial r$ , where  $\mathbf{e}_r$  is the unit vector in the streamwise direction, so  $(\tilde{\mathbf{u}} \cdot \nabla) f = \tilde{u} \partial f/\partial r$ . Dividing (2.9) by  $\partial \tilde{Y}/\partial r$  and using  $\tilde{\mathbf{u}} = \bar{\mathbf{u}} + \overline{\rho' u'}/\bar{\rho}$ , we obtain

$$- \frac{\partial \tilde{Y}/\partial t}{\partial \tilde{Y}/\partial r} = \bar{u} + \frac{1}{\bar{\rho}} \left( \overline{\rho' u'} + \frac{\nabla \cdot \overline{\rho Y'' \mathbf{u}''}}{\partial \tilde{Y}/\partial r} \right) - \frac{1}{\bar{\rho} \partial \tilde{Y}/\partial r} \nabla \cdot \left( \bar{\rho} D \frac{\partial \tilde{Y}}{\partial r} + \overline{\rho D \frac{\partial Y''}{\partial r}} \right) \mathbf{e}_r. \quad (2.10)$$

By combining (2.5) and (2.10), we obtain

$$\dot{R}|_{Y_0} = (\bar{u} + u_{Pen} + u_{Diff})|_{Y_0}, \quad (2.11)$$

where

$$u_{Pen} = \frac{1}{\bar{\rho}} \left( \overline{\rho' u'} + \frac{\partial \overline{\rho Y'' u''}}{\partial \tilde{Y}/\partial r} \right) + u_{Pen,G}, \tag{2.12a}$$

$$u_{Diff} = -\frac{1}{\bar{\rho}} \frac{\partial}{\partial \tilde{Y}/\partial r} \frac{\partial}{\partial r} \left( \bar{\rho} D \frac{\partial \tilde{Y}}{\partial r} + \overline{\rho D \frac{\partial Y''}{\partial r}} \right) + u_{Diff,G}. \tag{2.12b}$$

Here,  $\bar{u}|_{Y_0}$  is the Reynolds-averaged velocity at radius  $r$  with  $\tilde{Y}_l(r) = Y_0$ ;  $u_{Pen}$  describes the contribution of the fluctuation field,  $u_{Diff}$  represents the contribution of the molecular diffusion, and  $u_{Pen,G}$  and  $u_{Diff,G}$  are the terms caused by the spatial divergence in non-Cartesian coordinates, where

$$u_{Pen,G} = \frac{\alpha}{\bar{\rho}} \frac{\overline{\rho Y'' u''}}{\partial \tilde{Y}/\partial r}, \tag{2.13a}$$

$$u_{Diff,G} = -\frac{\alpha}{\bar{\rho}} \frac{1}{\partial \tilde{Y}/\partial r} \frac{1}{r} \left( \bar{\rho} D \frac{\partial \tilde{Y}}{\partial r} + \overline{\rho D \frac{\partial Y''}{\partial r}} \right), \tag{2.13b}$$

where  $\alpha$  is the geometry coefficient, with  $\alpha = 0, 1, 2$  for the Cartesian, cylindrical and spherical coordinates, respectively.

At two ends of the mixing zone, the term related to the fluctuation terms, i.e.  $u_{Pen,G}$ , is negligible compared with the terms related to the spatial gradient of the fluctuation terms (the validation can be found in figures 8 and 9). Combining (2.1) and (2.11), the growth rate of the mixing width is decomposed into

$$\dot{W} = \text{sgn}(A) \left[ (\bar{u}|_B - \bar{u}|_S) + (u_{Pen}|_B - u_{Pen}|_S) + (u_{Diff}|_B - u_{Diff}|_S) \right], \tag{2.14}$$

which is referred to as the decomposition formula. The formula indicates that the growth of the mixing width contains three parts.

- (i) The stretching or compression (S(C)) effect defined as the mean-velocity difference between two edges of the mixing zone, which is presented as the large arrows in figure 1. When this term is not zero, the mixing zone is stretched or compressed.
- (ii) The penetration effect defined by the fluctuating field. This effect is illustrated in figure 1 with small arrows. During the growth of the mixing zone,  $\overline{\rho Y'' u''}$  and  $\overline{\rho' u'}$  are dominated by two important processes: the light fluid penetrates the heavy fluid, and the heavy fluid penetrates the light fluid (Li *et al.* 2021).
- (iii) The diffusion effect caused by molecular diffusion, which tends to decrease the density gradient at the material interface.

According to the work of Li *et al.* (2021), the contribution of the diffusion effect is negligible in the flows at a high Reynolds number. Therefore, in the present work, we consider only the penetration effect and the S(C) effect.

The decomposition formula provides a method to analyse quantitatively the mechanisms controlling the evolution of the mixing width in interfacial fluid mixing. In the planar geometry, the perturbation growth caused by RT/RM instability is attributed to the penetration effect in most cases, while the S(C) effect, which is a growth mechanism independent of RM/RT growth, is significant only when the mixing zone is influenced by wave systems, such as shock, rarefaction and compression waves (Li *et al.* 2021). However,

## Stretching/compression in convergent RM instability

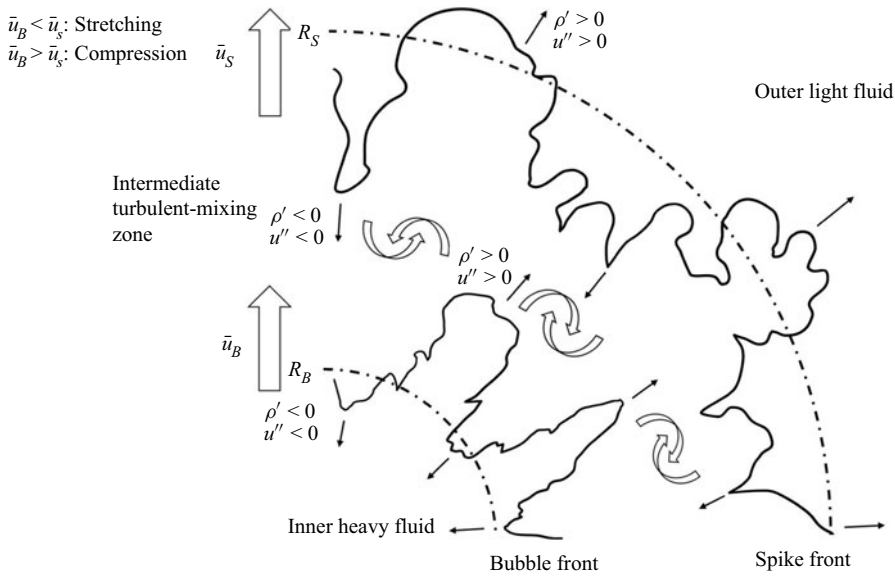


Figure 1. Schematic diagram of the growth of the mixing width in convergent geometry. The large arrows represent the mean velocity calculated at the bubble front and spike front. The small arrows represent the fluctuating velocity of the bubble and spike.

in the convergent geometry, the S(C) effect is evident even when there is no wave in the mixing zone (Ge *et al.* 2020). Therefore, the S(C) effect is an important difference between the interfacial mixing in planar geometry and that in convergent geometry.

### 2.2. Quantitative analysis of the S(C) effect

In this subsection, we consider the S(C) effect in planar, cylindrical and spherical geometries. For the fluids inside and outside the interface, the compression rates are assumed to be uniform around the interface, i.e.

$$\gamma_{\rho,in} = -\dot{\rho}_{in}/\rho_{in}, \quad \gamma_{\rho,out} = -\dot{\rho}_{out}/\rho_{out}. \quad (2.15a,b)$$

The works of Bell (1951) and Epstein (2004) are inherited in the present work, where the fluid motion is assumed to be irrotational. Therefore, there exist velocity potentials  $\Phi_{in/out}$  that satisfy a Poisson-type equation,  $\Delta\Phi_{in/out} = -\gamma_{\rho,in/out}$ . The initial perturbation is formulated as a single mode with a small amplitude. These results give the velocity potentials inside and outside the interface expressed as

$$\Phi_{in/out}(r, y, t) = \Psi_{in/out}(r, t) + \psi_{in/out}(r, y, t) \quad (2.16a)$$

in Cartesian coordinates  $(r, y)$ ,

$$\Phi_{in/out}(r, \theta, t) = \Psi_{in/out}(r, t) + \psi_{in/out}(r, \theta, t) \quad (2.16b)$$

in cylindrical coordinates  $(r, \theta)$ , and

$$\Phi_{in/out}(r, \theta, \varphi, t) = \Psi_{in/out}(r, t) + \psi_{in/out}(r, \theta, \varphi, t) \quad (2.16c)$$

in spherical coordinates  $(r, \theta, \varphi)$ . For the planar and cylindrical geometries, we disregard the  $z$ -dependent direction. The potential functions  $\Psi_{in/out}(r)$  describe the background flow

inside and outside the interface in all geometries, which are represented respectively as

$$\Psi_{in/out}(r, t) = -(r - R)\dot{R} - (r - R)^2 \frac{\gamma_{\rho, in/out}}{2} \quad (2.17a)$$

in the planar geometry,

$$\Psi_{in/out}(r, t) = -\left(R\dot{R} - \frac{R^2}{2} \gamma_{\rho, in/out}\right) \ln r - \frac{\gamma_{\rho, in/out}}{4} r^2 \quad (2.17b)$$

in the cylindrical geometry, and

$$\Psi_{in/out}(r, t) = \left(R^2\dot{R} - \frac{R^2}{3} \gamma_{\rho, in/out}\right) \frac{1}{r} - \frac{\gamma_{\rho, in/out}}{6} r^2 \quad (2.17c)$$

in the spherical geometry. For consistency, we use  $R$  to indicate the position of the interface throughout. Here,  $\psi_{in/out}$  represents the potential of the perturbed flow, which satisfies the Laplace function  $\Delta\psi_{in/out} = 0$  and thus is formulated as

$$\psi_{in/out}(r, y, t) = A_{in/out}(\gamma_{\rho, in/out}, t) \exp(\pm 2\pi mr/L) \cos(2\pi my/L) \quad (2.18a)$$

in the planar geometry (where  $m$  is the wavenumber of the perturbation, and  $L$  is the length scale in the spanwise direction  $y$ ),

$$\psi_{in/out}(r, \theta, t) = A_{in/out}(\gamma_{\rho, in/out}, t) r^{\pm m} \cos(m\theta) \quad (2.18b)$$

in the cylindrical geometry, and

$$\psi_{in/out}(r, \theta, \varphi, t) = A_{in/out}(\gamma_{\rho, in/out}, t) r^{[m, -(m+1)]} Y_m^n(\theta, \varphi) \quad (2.18c)$$

in the spherical geometry, where  $m - n$  and  $n$  are the latitude and longitude wavenumbers, respectively. Also,  $A_{in/out}(t)$  is the function determined by the boundary condition and is a function of only time. The perturbed interface equations are

$$r = R(t) + a(t) \cos(2\pi my/L) \quad (2.19a)$$

in the planar geometry,

$$r = R(t) + a(t) \cos(m\theta) \quad (2.19b)$$

in the cylindrical geometry, and

$$r = R(t) + a(t) Y_m^n(\theta, \varphi) \quad (2.19c)$$

in the spherical geometry, where  $a(t)$  is the amplitude of the perturbation. Therefore, the bubble front  $R_B$  and spike front  $R_S$  of the mixing zone are described as  $R - a$  and  $R + a$ , respectively. The Reynolds-averaged velocities at the bubble front and spike front in



different geometries are calculated as

$$\bar{u}_{B/S} = - \int_0^L \frac{\partial \Phi_{in/out}}{\partial r}(R_{B/S}, y) dy / \int_0^L dy \quad (2.20a)$$

in the planar geometry,

$$\bar{u}_{B/S} = - \oint_{\theta} \frac{\partial \Phi_{in/out}}{\partial r}(R_{B/S}, \theta) d\theta / \oint_{\theta} d\theta \quad (2.20b)$$

in the cylindrical geometry, and

$$\bar{u}_{B/S} = - \iint_{\theta, \varphi} \frac{\partial \Phi_{in/out}}{\partial r}(R_{B/S}, \theta, \varphi) d\theta d\varphi / \iint_{\theta, \varphi} d\theta d\varphi \quad (2.20c)$$

in the spherical geometry. As a result, we have

$$\bar{u}_S = \dot{R} + a\gamma_{\rho, out}, \quad (2.21a)$$

$$\bar{u}_B = \dot{R} - a\gamma_{\rho, in} \quad (2.21b)$$

in the planar geometry,

$$\bar{u}_S = \left( R\dot{R} - \frac{R^2}{2} \gamma_{\rho, out} \right) \frac{1}{R+a} + \frac{\gamma_{\rho, out}}{2} (R+a), \quad (2.21c)$$

$$\bar{u}_B = \left( R\dot{R} - \frac{R^2}{2} \gamma_{\rho, in} \right) \frac{1}{R-a} + \frac{\gamma_{\rho, in}}{2} (R-a) \quad (2.21d)$$

in the cylindrical geometry, and

$$\bar{u}_S = \left( R\dot{R} - \frac{R^2}{3} \gamma_{\rho, out} \right) \frac{1}{(R+a)^2} + \frac{\gamma_{\rho, out}}{3} (R+a), \quad (2.21e)$$

$$\bar{u}_B = \left( R\dot{R} - \frac{R^2}{3} \gamma_{\rho, in} \right) \frac{1}{(R-a)^2} + \frac{\gamma_{\rho, in}}{3} (R-a) \quad (2.21f)$$

in the spherical geometry. Substituting (2.21) into (2.14) and considering that  $a \ll R$ , one obtains that the S(C) effect is formulated as

$$\dot{W}_{S(C)} = (\alpha\gamma_R + \gamma_{\rho})W, \quad (2.22)$$

where  $\gamma_{\rho} = (\gamma_{\rho, out} + \gamma_{\rho, in})/2$ , the averaged compression rate, and  $W = 2a$  denotes the mixing width. The geometrical coefficient is  $\alpha = 0, 1, 2$  for the planar, cylindrical and spherical geometries, and  $\dot{W}_{S(C)} > 0$  means that the mixing zone is stretched, while  $\dot{W}_{S(C)} < 0$  means that the mixing width is compressed.

The interface convergence gives  $\gamma_R > 0$ , and fluid compression gives  $\gamma_{\rho} < 0$ . Therefore, the geometrical convergence leads to the stretching of the mixing zone, while fluid compression leads to the compression of the mixing zone. The coupling of geometrical convergence and fluid compression is realized by the linear superposition. Furthermore, in cylindrical geometry  $\alpha = 1$ , while in spherical geometry  $\alpha = 2$ . Therefore, the contribution from the geometrical convergence is more significant in the spherical geometry.

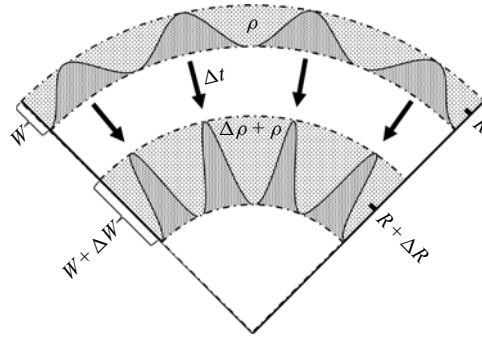


Figure 2. Schematic diagram of the S(C) effect. At time  $t$ , the mixing zone is positioned in the radius  $R$  with width  $W$ , where  $R$  is the centre radius of the mixing zone. The density  $\rho$  in the mixing zone is assumed to be uniform. After  $t + \Delta t$ , the mixing zone converges to radius  $R + \Delta R$  with width  $W + \Delta W$  and density  $\rho + \Delta \rho$ .

### 2.3. Physical origin of the S(C) effect

According to (2.22), the S(C) effect is determined by three physical quantities:  $\gamma_R$ ,  $\gamma_\rho$  and  $W$ . As will be shown, the underlying physical origin of (2.22) is that the mass in the mixing zone is conserved except for the mass brought in by the penetration effect.

As shown in figure 2, the mass in the mixing zone is  $\rho V_t$  at time  $t$ , and  $(\rho + \Delta \rho) V_{t+\Delta t}$  at time  $t + \Delta t$ . Here,  $V_t$  denotes the volume of the mixing zone at time  $t$ . In this demonstration,  $\rho$  is assumed to be uniform in the mixing zone. For the cylindrical geometry, we have  $V_t = \pi[(R + W/2)^2 - (R - W/2)^2] = 2\pi WR$ , where the axial length is unity. For the spherical geometry, we have  $V_t = (4\pi/3)[(R + W/2)^3 - (R - W/2)^3] = 4\pi WR^2(1 + W/12R)$ . By assuming that the mass in the mixing zone is conserved, we have  $\rho V_t = (\rho + \Delta \rho) V_{t+\Delta t}$ , i.e.

$$2\pi \rho WR = 2\pi (\rho + \Delta \rho) (W + \Delta W) (R + \Delta R) \tag{2.23a}$$

in the cylindrical geometry, and

$$4\pi \rho WR^2 \left(1 + \frac{W}{12R}\right) = 4\pi (\rho + \Delta \rho) (W + \Delta W) (R + \Delta R)^2 \left(1 + \frac{W + \Delta W}{12(R + \Delta R)}\right) \tag{2.23b}$$

in the spherical geometry. In most cases, the radial length of the mixing zone is much smaller than the radius. Therefore,  $W/12R \ll 1$ . By disregarding small quantities of any order higher than the first, we obtain

$$\Delta W = - \left( \frac{\Delta \rho}{\rho} + \alpha \frac{\Delta R}{R} \right) W, \tag{2.24}$$

where  $\alpha = 1, 2$  for the cylindrical geometry and spherical geometry, respectively. Dividing (2.24) by  $\Delta t$  and applying  $\Delta t \rightarrow 0$ , we have  $\dot{W}_{S(C)} = (\alpha \gamma_R + \gamma_\rho) W$ , which is the same as (2.22). Therefore, we verify that the S(C) effect originates from the idea that the mass in the mixing zone is conserved if we do not consider the mass brought in by the penetration effect. When the mixing zone undergoes fluid compression or interface convergence, the density or the spanwise length of the mixing zone changes, and the mixing width changes as well.

2.4. The S(C) effect and the BP effect

According to (2.22), the S(C) effect is caused by the geometrical convergence and fluid compression. For the geometrical convergence, it happens in only cylindrical and spherical geometries. For the fluid compression, it happens in a convergent system where the fluids are compressed, or when the mixing zone is influenced by waves, such as shock waves, rarefaction waves and compression waves. Therefore, we know that in planar geometry,  $\dot{W}_{S(C)} = 0$  when there is no wave system acting on the mixing zone (Li *et al.* 2021), while  $\dot{W}_{S(C)} \neq 0$  in convergent geometries (Ge *et al.* 2020). Therefore, we conclude that the S(C) effect is an important part of the BP effect.

However, the S(C) effect is not equivalent to the BP effect. The BP effect is, in fact, a collective factor for the modification caused by the geometry, which contains multiple mechanisms. For example, as the interface converges, the wavelength of the perturbations changes, and how this factor modifies the instability remains an open question.

In this section, we give the definition of the S(C) effect in (2.14). The quantitative relation between the S(C) effect and the geometrical convergence and fluid compression is given in (2.22), which implies that the S(C) effect originates from the conservation of the mixing mass. Furthermore, we prove that the S(C) effect is one of the mechanisms of the BP effect. In the next section, a series of numerical simulations is provided to support our theoretical analysis.

3. Numerical approach and problem set-up

3.1. Governing equations and computational approach

The flow field is governed by the compressible multi-component Navier–Stokes equations. The mass, momentum, energy and mass fraction equations are

$$\frac{\partial \rho}{\partial t} + \nabla \cdot (\rho \mathbf{u}) = 0, \tag{3.1a}$$

$$\frac{\partial \rho \mathbf{u}}{\partial t} + \nabla \cdot (\rho \mathbf{u} \mathbf{u}) = -\nabla \cdot (p \boldsymbol{\delta} - \boldsymbol{\tau}), \tag{3.1b}$$

$$\frac{\partial \rho E}{\partial t} + \nabla \cdot (\rho E \mathbf{u}) = -\nabla \cdot \left( p \mathbf{u} - \boldsymbol{\tau} \cdot \mathbf{u} - \kappa \nabla T - T \sum_i C_{p,i} (\rho D \nabla Y_i) \right), \tag{3.1c}$$

$$\frac{\partial \rho Y_i}{\partial t} + \nabla \cdot (\rho Y_i \mathbf{u}) = \nabla \cdot (\rho D \nabla Y_i), \tag{3.1d}$$

where  $\rho$ ,  $\mathbf{u}$ ,  $p$ , and  $T$  are the density, velocity vector, pressure and temperature, respectively. The energy of the fluid is  $E = e + \mathbf{u} \cdot \mathbf{u}/2$ , where  $e$  is the internal energy, and  $\mathbf{u} \cdot \mathbf{u}/2$  is the kinetic energy. Here,  $\boldsymbol{\delta}$  is the Kronecker function,  $Y_i$  is the mass fraction of the  $i$ th species, where  $i = 1, 2$  and  $Y_1 + Y_2 = 1$ ,  $\kappa$  and  $D$  are the mixture thermal conductivity and the mixture diffusion coefficient, respectively, and  $C_{p,i}$  is the constant-pressure-specific heat capacity of the  $i$ th species. To close the equations, the fluids are assumed to be Newtonian to calculate the shear stress, and the equations of state for the ideal gas are applied, i.e.

$$\boldsymbol{\tau} = \mu \left( \nabla \mathbf{u} + (\nabla \mathbf{u})^T - \frac{2}{3} \boldsymbol{\delta} (\nabla \cdot \mathbf{u}) \right), \tag{3.2a}$$

$$\frac{p}{\rho} = \frac{e}{\gamma - 1}, \tag{3.2b}$$

where  $\gamma = C_p/C_V$  is the heat capacity ratio, and  $C_V$  is the constant-volume-specific heat capacity.

The viscosity, thermal conductivity, and diffusivity of the  $i$ th species, which describe the physical properties of the component, are obtained as (Sutherland 1893),

$$\mu_i = \mu_{0,i} \left( \frac{T}{T_0} \right)^{3/2} \frac{T_0 + T_s}{T + T_s}, \tag{3.3a}$$

$$\kappa_i = C_{p,i} \frac{\mu_i}{Pr_i}, \tag{3.3b}$$

$$D_i = \frac{\mu_i}{\rho_i Sc_i}, \tag{3.3c}$$

where  $\mu_{0,i}$  is the viscosity at a reference temperature  $T_0 = 273.15$  K,  $T_s = 124$  K is an effective temperature (Li *et al.* 2019), and  $Pr_i$  and  $Sc_i$  are the Prandtl number and Schmidt number for the  $i$ th species, respectively.

The thermodynamic quantities  $f$  of the mixture in a computational cell are calculated following Reckinger, Livescu & Vasilyev (2016):

$$f = \begin{cases} \sum_i f_i, & \text{for } f = \rho, p, \\ f_1 = \dots = f_i, & \text{for } f = T, V, \\ \sum_i Y_i f_i, & \text{for } f = \mu, \kappa, D, C_V, C_p. \end{cases} \tag{3.4}$$

The governing equations are solved numerically by the finite difference method with the program APEX (Adaptive-mesh-refinement Program of Eulerian solvers with X-physics). To show the reliability in simulating RM instability with APEX, we simulate the case taken from the work of Thornber *et al.* (2017). Appendix A shows the numerical results and their comparison with other algorithms. The fifth-order weighted essentially non-oscillation (WENO) scheme is adopted for spatial reconstruction. The Harten–Lax–van Leer contact (HLLC) approximate Riemann solver is applied to calculate the convection flux. The time advancement is achieved through a third-order Runge–Kutta scheme.

### 3.2. Initial problem set-up

#### 3.2.1. Computational domain

In this subsection, we first simulate the RM instability in a cylindrical geometry. To compare the influence of geometry, RM instability in a planar geometry is also simulated, in which the perturbed interface is the same as that unfolded from the cylindrical interface. Both two-dimensional (2-D) and three-dimensional (3-D) cases are simulated. All cases are simulated under Cartesian grids ( $(x, y)$  for 2-D cases, and  $(x, y, z)$  for 3-D cases). The 2-D views of both configurations are depicted in figure 3. By comparing the subsequent growth of the perturbations on the two interfaces after shock time  $t_0$ , we can evaluate the influence caused by the geometry.

The initial setting of the cylindrical case is shown in figure 3(a). At the initial time  $t^-$ , the material interface is located at the position  $r = R_0$ . The convergent shock wave radius

Stretching/compression in convergent RM instability

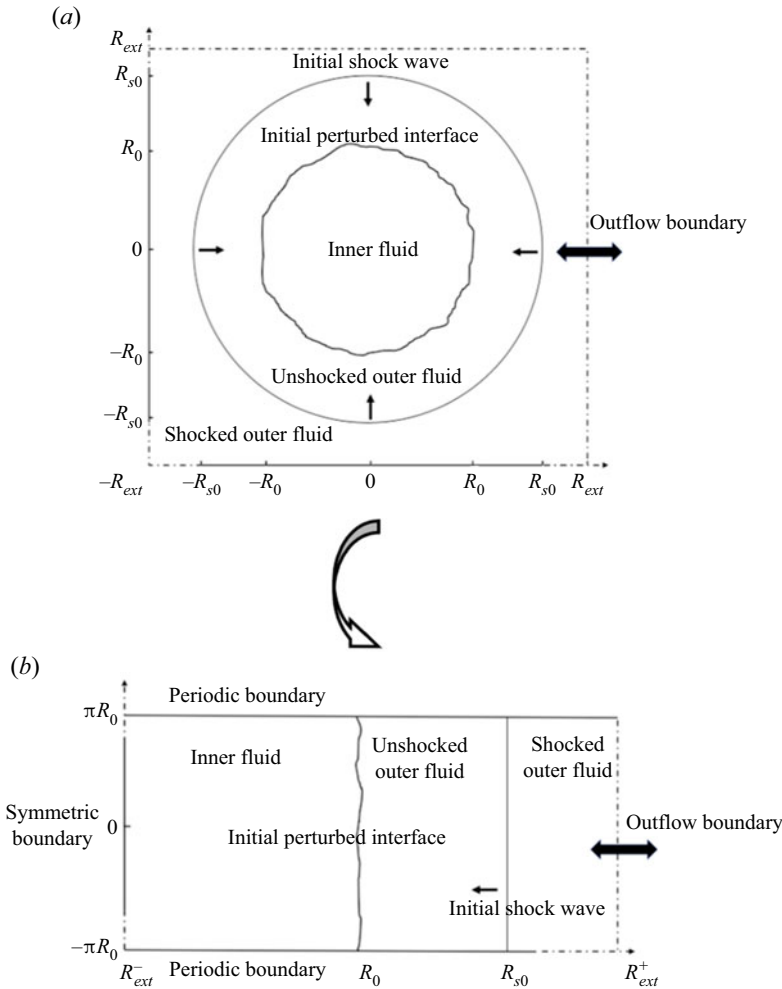


Figure 3. Planar slice at  $z = 0$  for (a) cylindrical geometry and (b) planar geometry.

is  $R_s(t^-) = R_{s0} = 1.1R_0$ , and the domain size  $\mathcal{V}_{cylinder}$  is

$$\mathcal{V}_{cylinder,2-D} = \{(x, y) \mid |x| \leq R_{ext}, |y| \leq R_{ext}\}, \quad (3.5a)$$

$$\mathcal{V}_{cylinder,3-D} = \{(x, y, z) \mid |x| \leq R_{ext}, |y| \leq R_{ext}, |z| \leq \pi R_0\}, \quad (3.5b)$$

with  $R_{ext} = 4\pi R_0$  to avoid possible influence caused by the boundaries. The symmetric boundaries are set in the axial direction  $z$ , while outflow conditions are applied in the  $x$  and  $y$  directions. The convergence analysis of the size of the computational domain is presented in [Appendix B](#).

The initial setting of the planar case is shown in [figure 3\(b\)](#). The planar interface is obtained by unfolding the cylindrical interface, including the perturbations. The planar case considered is a shock tube with a constant cross-section. At the initial time  $t^-$ , the material interface is located at the position  $x = R_0$ . The initial shock wave locates

Quantity	Fluid 1 (air)	Fluid 2 (SF <sub>6</sub> -acetone)
$\rho$ (kg m <sup>-3</sup> )	0.279	1.086
$p$ (kPa)	23.000	23.000
$T$ (K)	286.000	286.000
$ \mathbf{u} $ (m s <sup>-1</sup> )	0	0
$\mu_0$ ( $\times 10^{-5}$ kg m <sup>-1</sup> s <sup>-1</sup> )	1.716	1.239
$Pr$	0.720	0.800
$Sc$	0.757	0.691
$\gamma$	1.400	1.100

Table 1. The preshock state parameters and other properties of fluid 1 (air) and fluid 2 (SF<sub>6</sub>-acetone).

at  $R_s(t^-) = R_{s0}$ , and the domain size  $\mathcal{V}_{plane}$  is

$$\mathcal{V}_{plane,2-D} = \{(x, y) \mid R_{ext}^- \leq x \leq R_{ext}^+, |y| \leq \pi R_0\}, \quad (3.6a)$$

$$\mathcal{V}_{plane,3-D} = \{(x, y, z) \mid R_{ext}^- \leq x \leq R_{ext}^+, |y| \leq \pi R_0, |z| \leq \pi R_0\}, \quad (3.6b)$$

where  $R_{ext}^+ - R_{ext}^- = 2R_{ext}$ . We adjust  $R_{ext}^-$  to make sure that the re-shock time when the reflected shock wave impacts the interface is identical in the two geometries. An outflow boundary condition is applied at  $x = R_{ext}^+$ , while a symmetric boundary condition is used at  $x = R_{ext}^-$ . Periodic boundaries are applied in the  $y$  direction. The boundaries in the  $z$  direction are symmetric.

The streamwise direction refers to the direction in which the shock wave propagates, i.e. the radial direction in the cylindrical cases, and the  $x$  direction in the planar cases. The spanwise direction denotes the direction perpendicular to the streamwise direction.

For the 2-D cylindrical cases, the base grid resolution is  $4096^2$ , and four additional levels of refinement with a factor of two are applied. The finest resolution is therefore  $65\,536^2$ , i.e.  $\Delta x_{min} \approx 3.8 \times 10^{-4} R_0$ . The same  $\Delta x_{min}$  and refinement level are applied for the planar cases, i.e. the base grid resolution is  $4096 \times 1024$  ( $x$  direction  $\times$   $y$  direction) for the 2-D planar cases. For the 3-D cylindrical cases, the base grid resolution is  $512 \times 512 \times 128$  ( $x$  direction  $\times$   $y$  direction  $\times$   $z$  direction), and five additional levels of refinement with a factor of two are applied. The finest resolution is therefore  $16\,384 \times 16\,384 \times 4096$ , i.e.  $\Delta x_{min} \approx 1.5 \times 10^{-3} R_0$  in both domains. The same  $\Delta x_{min}$  and refinement level are applied for the planar cases, i.e. the base grid resolution is  $512 \times 128 \times 128$  for the 3-D planar cases. The grid convergence analysis is presented in [Appendix B](#).

### 3.2.2. Initial fluid state

The two fluids considered here are air (fluid 1, outside the interface) and SF<sub>6</sub>-acetone mixtures (fluid 2, inside the interface). As with Tritschler *et al.* (2014), the unshocked state parameters and other properties of the two fluids are shown in [table 1](#).

For the cylindrical configuration, the initialization of the postshock fluid refers to the work of Chisnell (1998). In that work, by solving the mass, momentum and entropy equations for postshock symmetric flow, using an adiabatic ideal gas assumption, the self-similar solutions of  $\rho$ ,  $p$ ,  $\mathbf{u}$  are given in terms of  $\xi = r/R_s$ , where  $R_s$  is the radius of the shock wave. For both geometries, the preshock and postshock states satisfy the Rankine–Hugoniot conditions.

For the cylindrical geometry, the initial Mach number of the shock wave is set to ensure a large convergence ratio ( $C_r \sim 10$ ) before the interface is re-shocked. Meanwhile, the

non-dimensional duration (defined in the next section) when the interface converges with a quasi-steady velocity should be long enough so that the cylindrical and planar cases are comparable. Hence the initial Mach number of the cylindrical shock wave is set to be 2.

For the planar geometry, the Mach number is adjusted so that the velocity jump of the interface  $\Delta V$  impacted by the incident shock is the same as that in the cylindrical geometry. In the cylindrical geometry, when the shock wave arrives at the interface at  $r = R_0$ , the Mach number is greater than the Mach number at the initial time  $t^-$ , i.e.  $Ma(t_0) > Ma(t^-)$ . By referring to the work of Si *et al.* (2015), we can predict the Mach number of the convergent shock wave at the shock time  $t_0$ . Based on this theoretical value, the Mach number is adjusted slightly and it is finally set to be  $Ma_{plane} = 2.14$  in the numerical simulations.

### 3.2.3. Initial perturbations

Two types of initial perturbations are applied: (i) single-mode perturbation in 2-D cases, and (ii) multi-mode perturbation in 3-D cases.

The single-mode perturbations at both interfaces are presented as

$$\eta_{cylinder}(\theta) = a_m \cos(k_m \theta R_0) \tag{3.7}$$

and

$$\eta_{plane}(y) = a_m \cos(k_m y), \tag{3.8}$$

where  $a_m$  is the amplitude of perturbation, and  $k_m = mk_0$ , with  $m$  the wavenumber and  $k_0 = 2\pi/(2\pi R_0) = 1/R_0$ . Two wavenumbers are applied:  $m = 8$  and  $m = 16$ , which are named SP8 and SP16, respectively. The initial amplitude is  $a_m = 0.01\lambda_m$ , where  $\lambda_m = 2\pi R_0/m$ .

The multi-mode perturbation is a superposition of a series of modes with a prescribed power spectrum (Dimonte *et al.* 2004). The power spectrum is given as

$$P(k) = \begin{cases} Fk^l, & k_{min} < k < k_{max}, \\ 0, & \text{otherwise,} \end{cases} \tag{3.9}$$

where  $k = \sqrt{k_m^2 + k_n^2}$  denotes the wavenumber of the mode  $(m, n)$ , and  $F$  is the coefficient. In physical space, the perturbations are of the form

$$\begin{aligned} \eta_{cylinder}(\theta, z) = \sum_{m,n} (a_{mn} \cos(k_m \theta R_0) \cos(k_n z) + b_{mn} \sin(k_m \theta R_0) \cos(k_n z) \\ + c_{mn} \cos(k_m \theta R_0) \sin(k_n z) + d_{mn} \sin(k_m \theta R_0) \sin(k_n z)) \end{aligned} \tag{3.10}$$

and

$$\begin{aligned} \eta_{plane}(y, z) = \sum_{m,n} (a_{mn} \cos(k_m y) \cos(k_n z) + b_{mn} \sin(k_m y) \cos(k_n z) \\ + c_{mn} \cos(k_m y) \sin(k_n z) + d_{mn} \sin(k_m y) \sin(k_n z)), \end{aligned} \tag{3.11}$$

where the amplitude coefficients  $a_{mn}$ ,  $b_{mn}$ ,  $c_{mn}$  and  $d_{mn}$  are determined by the variance  $\sigma_{mn}^2 \sim P(k_m, k_n) \Delta k_m \Delta k_n$ , which corresponds to the energy involved in wave space, and  $k_m = mk_0$  and  $k_n = nk_0$ , where  $k_0 = 2\pi/(2\pi R_0) = 1/R_0$ . The relevant detailed demonstration of the transformation from the wave space (3.9) to the physical space (3.10) and (3.11) has been given by Thornber *et al.* (2010). In the present work, a narrowband

perturbation with wavenumbers ranging from 16 to 48 is used, and the energy spectrum follows  $P(k) = Fk^0$ . The total standard deviation is  $\sigma = \sqrt{\int P(k) dk} \approx 0.0067R_0$ . These cases are named MP16–48.

### 3.2.4. Summary of initial conditions

The initial conditions are designed carefully so that the RM instability on a planar interface and a cylindrical interface are comparable. A perturbed cylindrical interface and a planar interface obtained by unfolding the cylindrical interface are impacted by shock waves with the same strength. According to the RM linear model  $\dot{W} = A^+k \Delta V W^+$  in the planar geometry (Richtmyer 1960), where  $A^+$  and  $W^+$  are the postshock Atwood number and the postshock width of the perturbation, the perturbations in the two geometries should have the same initial growth rate. During the subsequent growth of the perturbations, whether the interface converges or not is the only independent variable, from which we can reasonably compare the difference in the perturbation evolution under the two geometries. Specifically, the set-ups need to meet the following conditions.

- (i) The initial preshock fluid states, the initial perturbations and the initial interface size are the same in both geometries.
- (ii) The Mach number in the planar geometry is larger than that in the cylindrical geometry at initial time  $t^-$  to ensure that the velocity jumps  $\Delta V$  impacted by the incident shock are equal in the two geometries.
- (iii) The convergence ratio  $C_r$  should be high, and the non-dimensional duration when the interface converges with a quasi-steady velocity should be long enough so that the cylindrical and planar cases are comparable. The re-shock time when the reflected shock wave impacts the interface should also be identical in the two geometries.

## 4. Numerical results

### 4.1. One-dimensional unperturbed flow

In this section, we inspect the one-dimensional unperturbed cases, with an emphasis on the periods before the re-shock moment  $t_{rs}$ . Figure 4 shows the interface motion  $R(t)$  in both geometries. The interface has a non-zero width because of the numerical diffusion, therefore the position of the interface  $R(t)$  is defined as the radius where  $Y_1(R(t), t) = 0.5$ . The curves obtained from the planar case are shifted along the time axis so that the shock time  $t_s$  is aligned. The interface is shocked at time  $t_s = 0.4$  ms, then the planar interface moves with a constant velocity  $\Delta V = 340$  m s<sup>-1</sup> until the interface is re-shocked at  $t_{rs} = 8.5$  ms. For the cylindrical case, before  $t_1 = 5$  ms, the convergence velocity is slightly increased, and after that, the interface begins to decelerate. At re-shock time  $t_{rs}$ , the final convergence ratio of the interface is  $C_r(t_{rs}) \sim 10$ .

The temporal evolution of the averaged fluid compression rate  $\gamma_\rho$  is plotted in figure 5, where the density value is sampled from two sides of the interface. At time  $t_s$ , the interface is shocked by the shock wave, which results in a strong compression of the fluids. For time  $t \in [t_s, t_0]$ , where  $t_0 = 1$  ms, the shock wave continues to affect the fluids near the interface, which results in the negative pulse of the fluid compression. After  $t_0$ , the planar RM flow is quasi-incompressible before the re-shock, which supports the discussion in § 2.4. Fluid compression is one of the basic features of convergent RM instability.



Stretching/compression in convergent RM instability

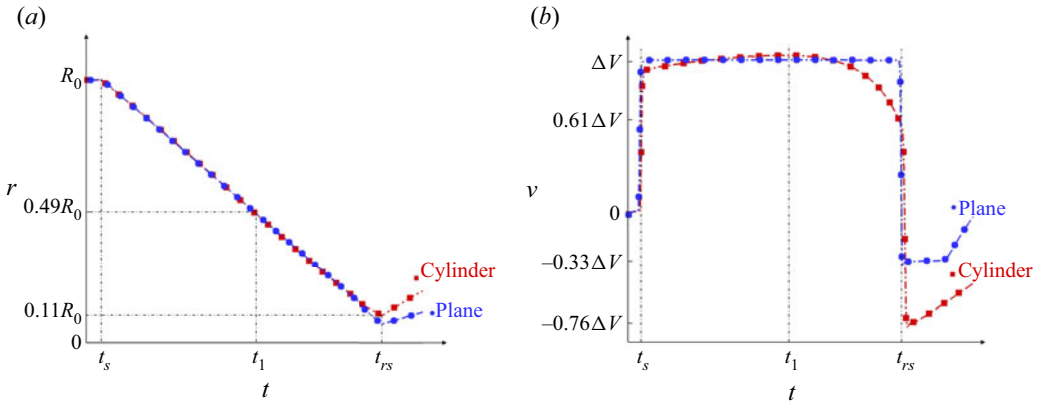


Figure 4. The displacement (a) and velocity (b) of the interface.

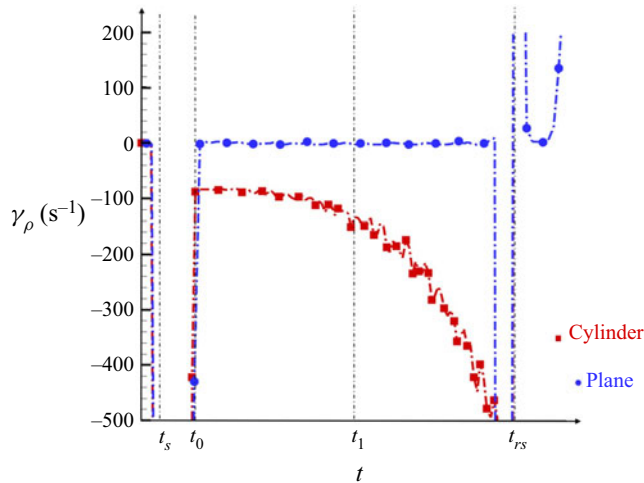


Figure 5. The temporal evolution of the fluid compression rate.

Therefore, for cylindrical cases, after  $t_0$ , a non-zero fluid compression rate can still be observed, and its absolute value continues to rise with the convergence of the interface.

According to the evolution of the fluid parameters mentioned above, the flow evolution is divided into five stages, as shown in table 2. Due to the nature of the convergent shock wave, the acceleration of the convergent interface is not zero. Therefore, the growth of perturbations in the convergent geometries is coupled with RT stability/instability. RT instability, as introduced in § 1, is the phenomenon where the perturbation grows in an acceleration environment (the lighter fluid accelerates the heavier fluid), while the RT stability is the situation when the heavier fluid accelerates the lighter fluid and the perturbations oscillates or attenuates.

The quantities presented in the following subsections are non-dimensionalized. For the single-mode cases, the characteristic length is the initial wavelength of the perturbation,  $L^* = \lambda$ . The characteristic velocity is  $V^* = A^+ k \Delta V W^+$ , where  $W^+ = (1 - \Delta V/V_s) W(t^-)$ , and  $V_s$  is the velocity of the shock wave. For the multi-mode cases, the characteristic velocity is defined as the growth rate of the perturbations at time  $t_0$  when the shock wave just passes away from the interface. The characteristic length is

Stage	Time duration	Description
I	$[t^-, t_s]$	The interface has not been shocked. All the preshock parameters in both geometries remain the same.
II	$[t_s, t_0]$	Shock phase, the interfaces are shocked with the same strength.
III	$[t_0, t_1]$	The interface converges at a slightly increased velocity.
IV	$[t_1, t_{rs}]$	The interface begins to decelerate.
V	$t_{rs}$	Re-shock. The convergence ratio is $C_r \sim 10$

Table 2. Definition of five stages of the RM instability until the re-shock time.

Case	Length $L^*$ (m)	Time $T^*$ (s)	Velocity $V^*$ (m s <sup>-1</sup> )
SP8	2.36	0.155	15.23
SP16	1.18	0.077	15.23
MP16–48	0.59	0.012	47.30

Table 3. Characteristic quantities for each case.

$L^* = \bar{\lambda}$ , where  $\bar{\lambda} = 2\pi/\bar{k}$  is the equivalent wavelength of the perturbations at time  $t^-$ , and  $\bar{k}$  is calculated by the energy-weighted average of  $k$ , which is formulated as

$$\bar{k} = \frac{\int_{k_{min}}^{k_{max}} k P(k) dk}{\int_{k_{min}}^{k_{max}} P(k) dk}. \tag{4.1}$$

In this paper,  $P(k) = Ck^0$ , hence  $\bar{k} = 0.5(k_{min} + k_{max})$ . The characteristic quantities for all of the cases are listed in [table 3](#).

#### 4.2. Single-mode cases

[Figures 6](#) and [7](#) show the growth of the perturbations for the cases SP8 and SP16, respectively. After  $\tau = \tau_0$  when the shock wave passes away from the interface, the initial growth rates are identical in both geometries, as designed in [§ 3](#). Because the initial amplitude of the perturbations is set as  $a_m = 0.01\lambda_m$ , the growth of the perturbations lies in the linear stage.

For the planar configurations, the growth rate of the perturbations increases slowly and is smaller than the growth rate predicted by the linear theory (Richtmyer 1960) by the time  $t_{rs}$ , i.e. the non-dimensional growth rate is smaller than 1. This shows that the growth of the perturbations is still in the start-up process (Lombardini & Pullin 2009). For the cylindrical configurations, the temporal evolution of the perturbation growth rate is significantly different from that of the planar configurations. The growth rate in the cylindrical geometry is first accelerated and then decelerated to a negative value. This complicated growth behaviour in the cylindrical geometry originates from the coupling of multiple physical effects (for example, the RT instability/stability, geometrical convergence, and fluid compression).

The decomposition formula (2.14) is applied to decompose the growth of the perturbations, where the contribution of the diffusion is neglected. The results are given

Stretching/compression in convergent RM instability

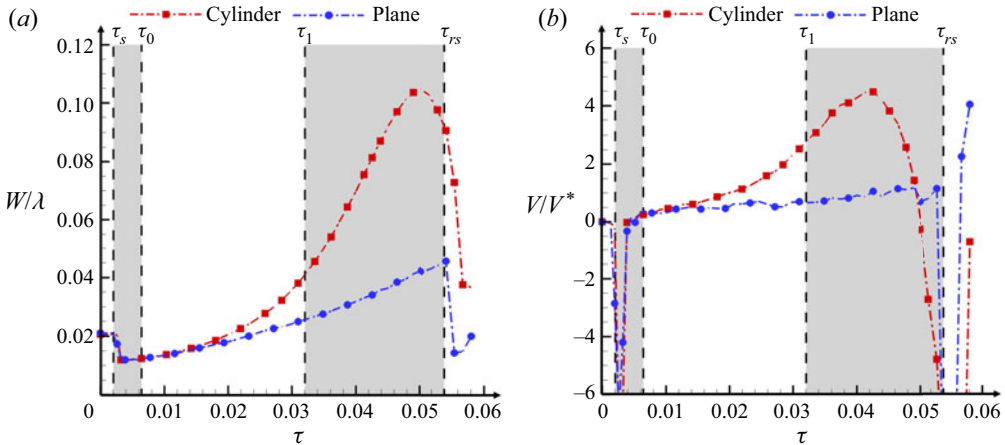


Figure 6. For the case SP8, the temporal evolution of the mixing width, as well as its growth rate, in both geometries.

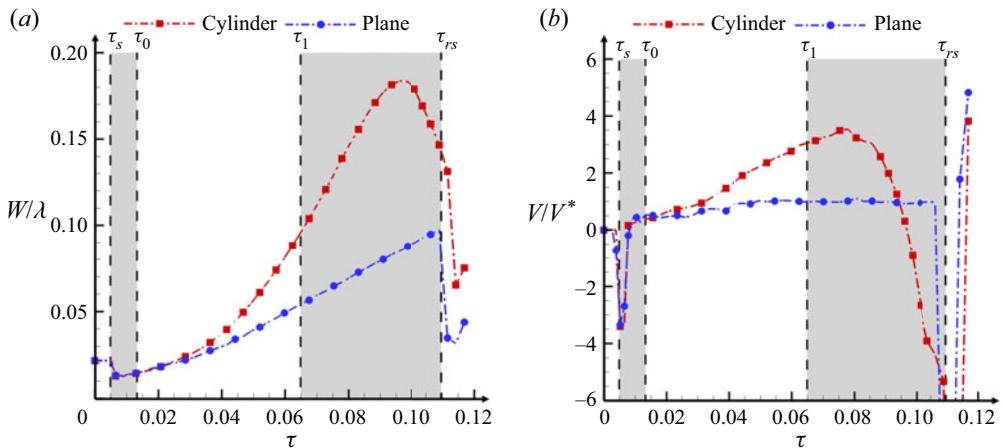


Figure 7. For the case SP16, the temporal evolution of the mixing width, as well as its growth rate, in both geometries.

in figures 8 and 9. In all configurations, the results obtained by the decomposition formula  $\dot{W}_{formula}$  and the results extracted directly from the numerical simulations  $\dot{W}_{sim}$  are consistent, which proves the reliability of the decomposition formula. Furthermore, in figures 8(b) and 9(b), we have  $\dot{W}_{Pen,G} = u_{Pen,G}|_B - u_{Pen,G}|_S \approx 0$ , where  $u_{Pen,G}$  is defined in (2.13), which is neglected in the following analysis.

For the planar cases, one can observe that  $\dot{W}_{S(C)}$ , which represents the contribution of the S(C) effect, is not zero only when the wave system acts on the mixing zone. For most of the time in the duration  $[\tau_0, \tau_{rs}]$ , the growth of the mixing width is dominated by the penetration effect, as shown in figures 8(a) and 9(a), which is consistent with the previous work of Li *et al.* (2021). For the cylindrical geometry, at the initial time,  $\dot{W}_{S(C)}(\tau_0) = 0$ . However, with the evolution of the flow, the contribution of the S(C) effect continues to increase and finally exceeds the penetration effect to dominate the growth of the perturbations. From the numerical results, we know that the S(C) effect is very

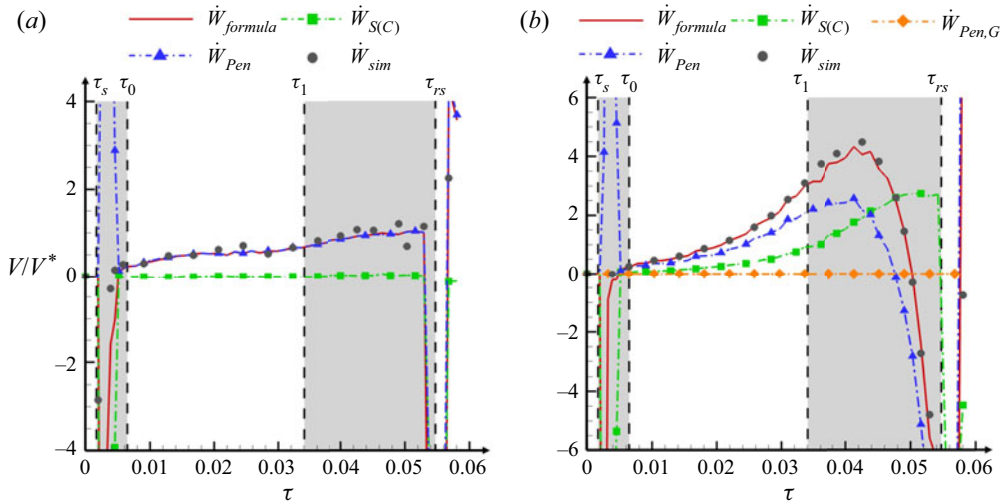


Figure 8. For the case SP8, the growth rates obtained by the simulation and the decomposition formula for (a) planar geometry and (b) cylindrical geometry.

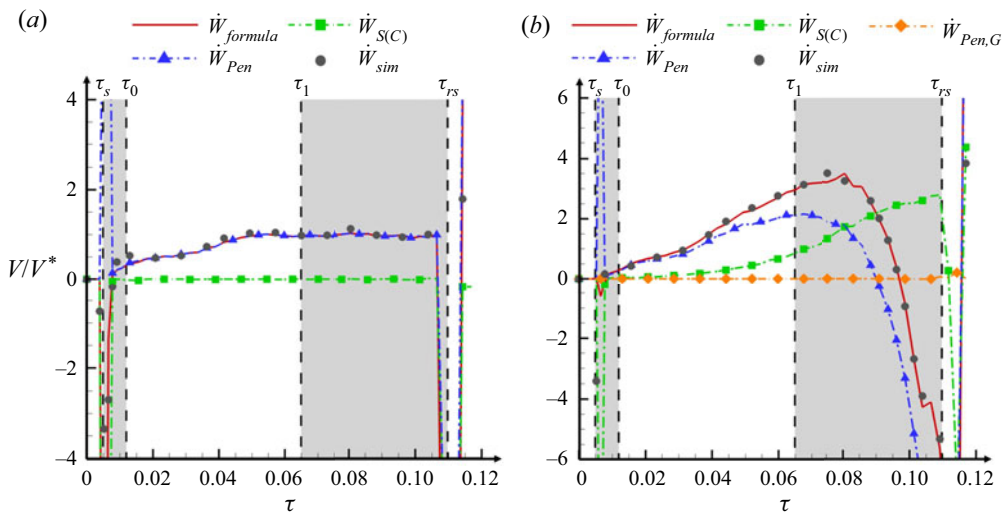


Figure 9. For the case SP16, the growth rates obtained by the simulation and the decomposition formula for (a) planar geometry and (b) cylindrical geometry.

different in the two geometries, therefore the S(C) effect is an important part of the BP effect.

The comparisons of the penetration effect are shown in figure 10. In both geometries, the  $\dot{W}_{Pen}$  values are identical at the initial time. With the coupling effect of geometrical convergence and the RT instability, the fluid penetration effect increases before the convergent velocity reaches its maximum  $\tau_1$ . After that, under the influence of the RT stability, the penetration rate decreases to a negative value at late time.

The evolution of the S(C) effects is shown in figure 11. The values of  $\gamma_\rho$  and  $\gamma_R$  used in (2.22) are obtained from the one-dimensional unperturbed simulations. The numerical results and the theory agree well, which proves the reliability of the theory.

### Stretching/compression in convergent RM instability

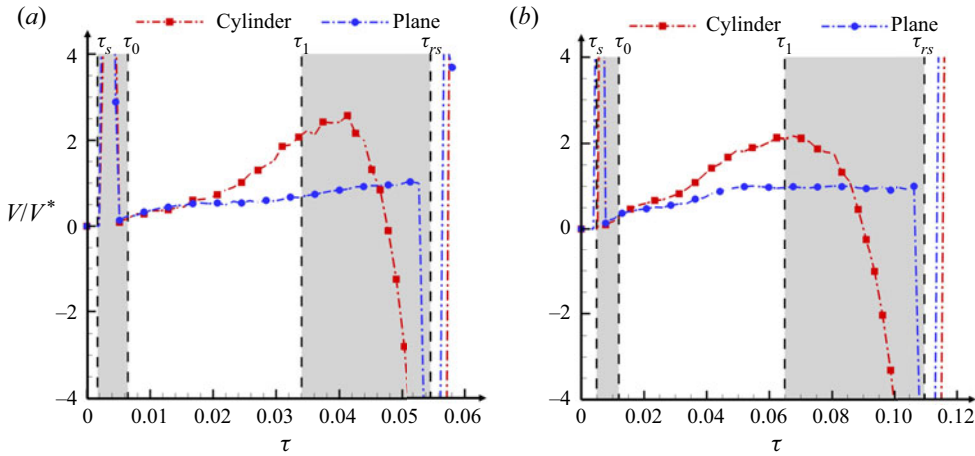


Figure 10. For (a) the case SP8 and (b) the case SP16, the different performances of the penetration effect in the two geometries.

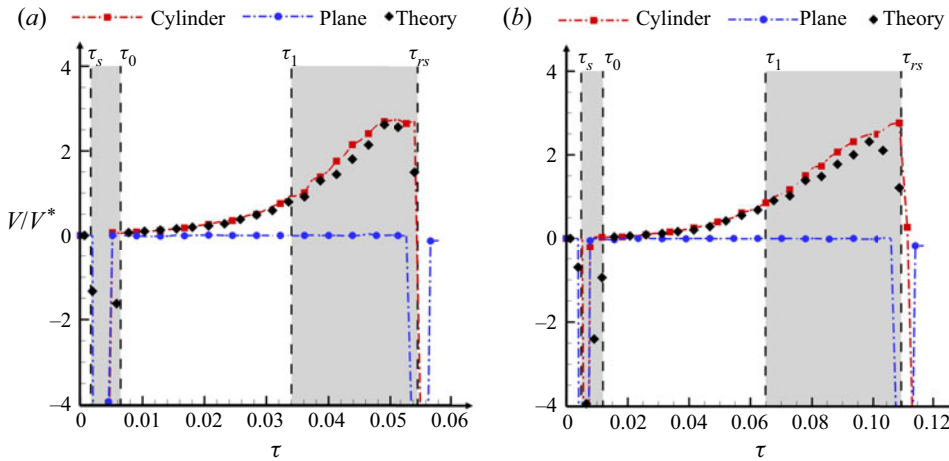


Figure 11. For (a) the case SP8 and (b) the case SP16, the evolution of the S(C) effect in the two geometries. The theoretical prediction for the S(C) effect in the cylindrical geometry is also shown.

The stretching effect ( $V_{Stretching} = \gamma_R W$ ) and the compression effect ( $V_{Compression} = \gamma_\rho W$ ) are given in figure 12. In the short duration  $\tau \in [\tau_s, \tau_0]$ , the perturbations are compressed strongly by the shock wave. Therefore, the S(C) effect is dominated by the compression effect caused by the shock wave. In the duration  $\tau \in [\tau_0, \tau_{rs}]$ , the stretching velocity is always greater than the compression velocity, with the ratio  $|V_{Stretching}/V_{Compression}|$  ranging from 1 to 2.

#### 4.3. Multi-mode case

To examine the universality of the results obtained from the single-mode cases, the multi-mode cases are simulated. Figure 13 gives the growth of the perturbations for the cases MP16–48. For the planar configuration, after  $\tau = \tau_0$ , there is no more energy injected into the system. Therefore, in the duration  $\tau \in [\tau_0, \tau_1]$ , the growth rate of the perturbations first experiences a short-time increase and then attenuates. For the

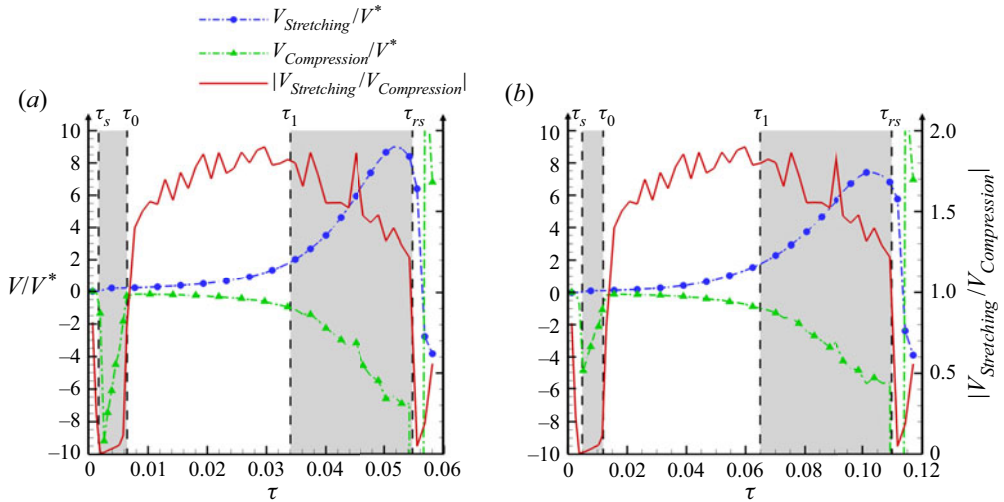


Figure 12. For (a) the case SP8 and (b) the case SP16, the contributions of different components in the S(C) effect of the cylindrical cases.

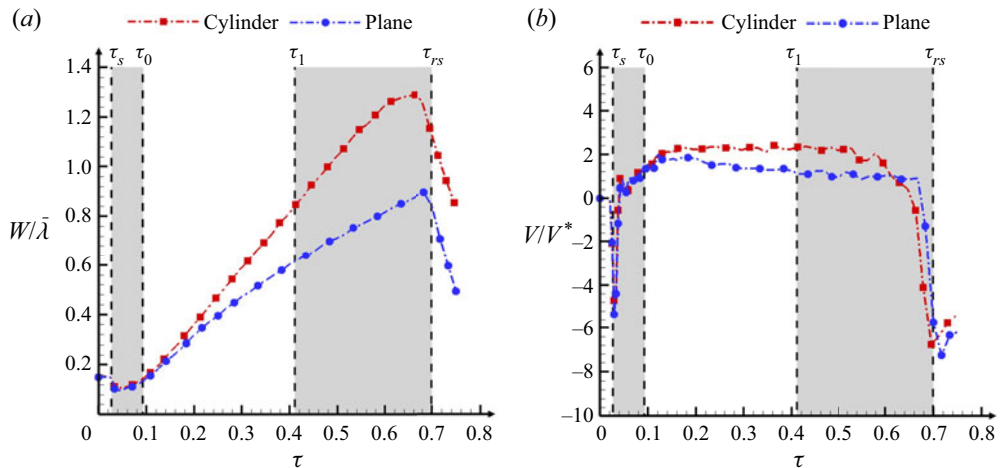


Figure 13. For the cases MP16–48, the temporal evolution of the mixing width, as well as its velocity, in both geometries.

cylindrical configuration, it is obvious that the convergent interface enhances the growth of the perturbations. In the duration  $\tau \in [\tau_0, \tau_1]$ , the growth rate of the perturbations does not decay, in contrast with that in the planar geometry. During the subsequent duration  $\tau \in [\tau_1, \tau_{rs}]$ , the acceleration of the interface is pointed from the heavy fluid to the light fluid; hence the growth of the perturbations is influenced by the RT stability, which decelerates the growth of the perturbations.

Figure 14 shows the growth rates obtained with the decomposition formula and those obtained from the numerical results in both geometries. In both geometries, at time  $\tau_s$  when the incident shock wave impacts the interface,  $\dot{W}_{S(C)}$  experiences a sharp decrease due to the compression by the shock wave. Meanwhile, the incidence shock wave deposits vorticity on the interface, which results in an increase in the penetration effect  $\dot{W}_{Pen}$ .

## Stretching/compression in convergent RM instability

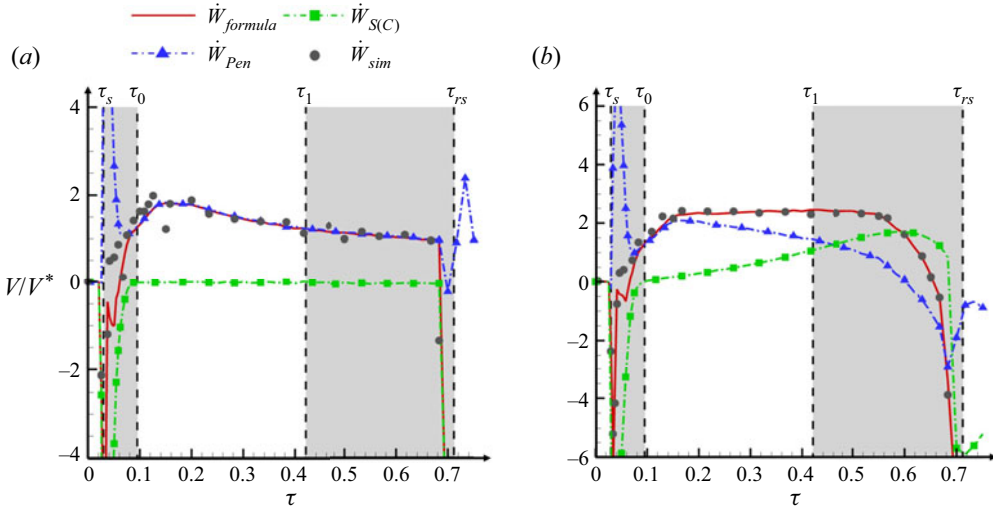


Figure 14. For the cases MP16–48, the growth rates obtained by the simulation and the decomposition formula for (a) planar geometry and (b) cylindrical geometry.

For the planar configuration,  $\dot{W}_{S(C)}$  is always zero when  $\tau \in [\tau_0, \tau_{rs}]$ , which indicates that the growth of the mixing width is dominated by the penetration effect if there is no influence of the wave system. For the cylindrical configuration, with the convergence of the interface, the stretching effect of the mixing width continues to increase. When  $\tau > \tau_1$ , the contribution of the penetration effect decreases due to the RT stability, while the stretching effect surpasses the penetration effect and begins to dominate the perturbation growth.

Figure 15(a) shows the evolution of the penetration effect in the two geometries. After the passage of the shock wave, as the initial growth rates are the same, the penetration rates in both geometries are identical. In the subsequent duration  $\tau \in [\tau_0, \tau_1]$ , the penetration rates increase first and then decay with almost the same rate in both geometries. This is because the growth of most perturbation modes enters the nonlinear phase. This phenomenon is different from the single-mode cases, for which the growth of the perturbations lies in the linear stage or the weakly nonlinear stage for most of the time. When  $\tau \in [\tau_1, \tau_{rs}]$ , the growth of the perturbations in cylindrical geometries is influenced by the RT stability. As a result, the penetration rate decays faster in cylindrical geometry than in planar geometry. In the late stage, the penetration effect is negative in cylindrical geometry, which indicates a reduction in the mixing width.

As shown in figure 15(b), the behaviour of the S(C) effect in the multi-mode case is similar to that in the single-mode cases. For the planar cases, the influence of the S(C) effect is observed only when the shock wave impacts the interface, while  $\dot{W}_{S(C)}$  increases with time in the cylindrical geometry. The ratio between the stretching effect and compression effect is also similar to the single-mode cases, as shown in figure 16.

### 5. Discussion

The numerical results presented in § 4 support our discussion in § 2 that the S(C) effect is an important part of the BP effect. Furthermore, as shown in § 4, for different geometries, there indeed exists a difference in the penetration effect, which verifies that the BP effect has in fact multiple mechanisms. Therefore, the S(C) effect is an important part of the

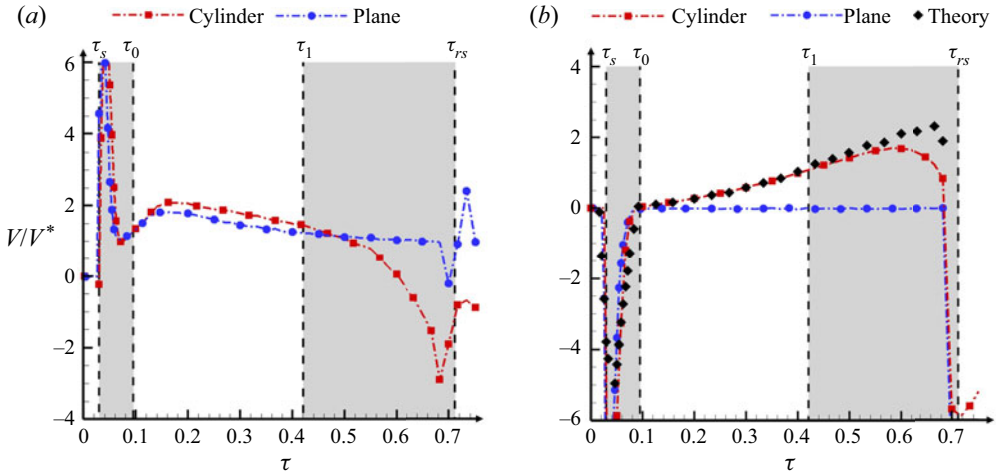


Figure 15. For the cases MP16–48, the different performance of (a) the penetration effect and (b) the S(C) effect, in the two geometries. The theoretical prediction of the S(C) effect is also shown.

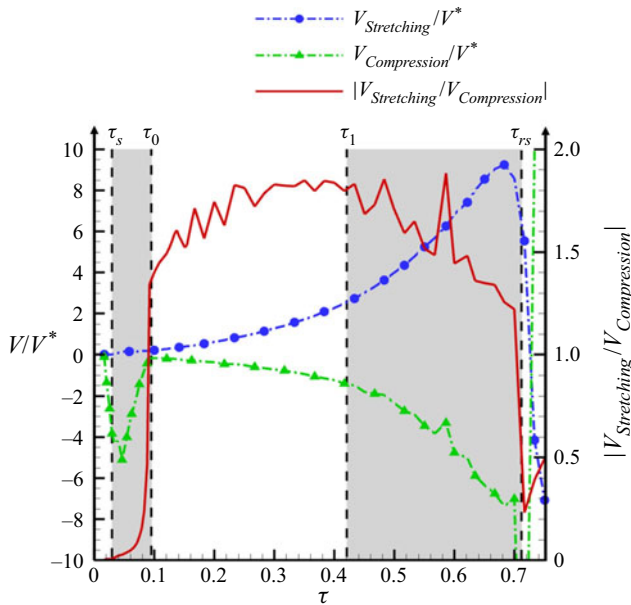


Figure 16. For the cases MP16–48, the contribution of different components in the S(C) effect of the cylindrical geometry.

BP effect but not equivalent to the BP effect. Because of the non-zero acceleration in the cylindrical interface, it is hard to evaluate the modification in the penetration effect caused by the BP effect. For our single-mode cases, the growth of perturbation is mainly in the linear and weakly nonlinear phase, and the difference in the penetration effect is obvious. However, in our multi-mode cases, the perturbations grow rapidly into the nonlinear phase. In the duration  $\tau \in [\tau_0, \tau_1]$  when there is no strong RT instability, it is remarkable that the main difference between the growths of the perturbations in the two geometries is contributed by the S(C) effect, and that there is little difference in the penetration effect. In



physical reality, the perturbations are always multi-mode, which contains a wide range of modes. Therefore, the results of single-mode cases can be referred to so as to understand the evolution of the low-order modes, while the results of the multi-mode cases can be referred to in order to understand the evolution of the high-order modes. However, the quantitative analysis of the perturbation growth in reality needs further investigations, especially for the penetration effect.

The S(C) effect can explain the phenomenon of the ‘thickening smooth premixing layer’ in the LANL experiments (Lanier *et al.* 2003). Since there is no penetration effect for the smooth premixing layer, the mixing layer thickens because of the S(C) effect. The theoretical results of the S(C) effect in different geometries (2.22) does not include explicitly the initial perturbations, interface acceleration and Atwood number. Moreover, as shown in § 4, (2.22) is applicable for different forms of initial perturbations and all stages of flow evolution.

As the S(C) effect is the mechanism independent to the penetration effect, this part of the contribution should be considered additionally in constructing models for the growth of mixing width in the convergent geometries. For example, El Rafei & Thornber (2020) propose a buoyancy-drag model for the RM instability in the spherical geometry to model the mixing-zone width, where the ‘BP effect’ is taken into account in ‘bubble and spike velocities ( $V_b, V_s$ ) relative to the fluid’. Mathematically,  $V_b, V_s$  are calculated as

$$V_b = \frac{dh_b}{dt} - (U_b - U_I), \quad (5.1a)$$

$$V_s = \frac{dh_s}{dt} - (U_I - U_s), \quad (5.1b)$$

where  $U_b, U_s$  and  $U_I$  are determined from one-dimensional results at the bubble front, spike front and interface, respectively (El Rafei & Thornber 2020). Essentially, the second term on the right-hand side of each equation in (5.1) can be explained as eliminating the S(C) effect.

## 6. Conclusions

The S(C) effect, which is induced by the velocity difference between two ends of the mixing zone, is defined based on the decomposition formula for the growth of the mixing width. Starting from the linear theory, the quantitative relationship between the S(C) effect and the flow parameters is given. The physical origin of the S(C) effect and the relationship between the S(C) effect and the BP effect are discussed. A series of numerical simulations in cylindrical and planar geometries is performed to describe modifications of RM instability induced by the geometry. To ensure that the numerical cases in the two geometries are comparable, the perturbed planar interface is obtained by unfolding the perturbed cylindrical interface. The preshock flow states are identical in both geometries. Moreover, both interfaces are impacted by a shock wave of the same strength. The convergence ratio of the cylindrical cases  $C_r \sim 10$  makes sure that the BP effect is shown clearly. The conclusions are listed below.

- (i) The S(C) effect in planar, cylindrical and spherical geometries is evaluated as  $\dot{W}_{S(C)} = (\alpha\gamma_R + \gamma_\rho)W$  in (2.22). Further analysis about (2.22) shows that when there is no wave acting on the mixing zone,  $W_{S(C)} = 0$  in the planar geometry while  $W_{S(C)} \neq 0$  in convergent geometries. Therefore, we conclude that the S(C) effect is an important part of the BP effect.

- (ii) The physical origin underlying the S(C) effect is that the mass in the mixing zone is conserved if we do not consider the mass brought in by the penetration effect.
- (iii) Both the decomposition formula and the theoretical expression of the S(C) effect agree well with the corresponding numerical results. This agreement is valid for a wide range of initial perturbations and different evolution stages. In the present cases, the contribution of the geometrical effect is always greater than the fluid compression, except for the duration when the shock wave impacts the mixing zone. Therefore, the mixing zone is always stretched.
- (iv) The penetration effect is different in the two geometries. Therefore, the S(C) effect is not equivalent to the BP effect. In the present work, the quantitative comparison of the penetration effect in the two geometries is hard because of the existence of the RT stability/instability. The modification on the penetration effect caused by the geometry remains an open question.
- (v) The S(C) effect is a growth mechanism that is independent of the RM and RT instabilities (Li *et al.* 2021). Therefore, for the RM/RT instability in a convergent geometry, additional consideration needs to be given to the stretching or compression of the mixing zone when we model the mixing width by the bubble/spike dynamics (such as the buoyancy-drag model) or extend the understanding in the planar geometry to the convergent geometry.

In the present work, the lighter fluid locates in the outside of the interface, i.e. the initial shock wave propagates from the light fluid to the heavy fluid. For the opposite configuration where the lighter fluid is in the inside, the growth of the perturbation will experience a phase-reversal process, i.e. the amplitude of the perturbation first decreases and then increases in the opposite direction. This process occupies a considerable part of the comparable time, which will influence the comparison between the two geometries. This is why we choose the configuration to put the lighter fluid on the outside. However, the comparison of RM instability in planar and cylindrical geometries where the lighter fluid is in the inside of the interface is still important work worthy of future investigation.

**Funding.** The authors acknowledge financial support from the National Natural Science Foundation of China (B.T., grant no. 91852207), (H.L., grant no. 11802038). The authors want to extend thanks for the Tianhe-2 computing resources supported by the group of Professor C.-B. Li from Peking University.

**Declaration of interests.** The authors report no conflict of interest.

**Author ORCID.**

 Jin Ge <https://orcid.org/0000-0002-6089-4750>;

 Haifeng Li <https://orcid.org/0000-0002-2651-6086>.

## Appendix A. Validation of APEX

In the work of Thornber *et al.* (2017), eight independent algorithms were employed to test a standard RM problem with multi-mode perturbations. The mathematical expression of the initial perturbations is the same as (3.9). In this problem, The computational domain is Cartesian and measures  $x \times y \times z = 2.8\pi \times 2\pi \times 2\pi \text{ m}^3$ . The initial wavelength is  $\lambda \in [L/8, L/4]$ , where  $L$  is the length of the cross-section. The distribution of energy is  $P(k) = Ck^0$ . The total standard deviation is  $\sigma = \sqrt{\int P(k) dk} = 0.1\lambda_{min}$ , where  $\lambda_{min} = L/8$ . The initial pre-mixing width is  $\delta = L/32$ . The initial Atwood number is  $A = 0.5$ . The shock wave propagates from the light fluid to the heavy fluid. As a result, the numerical results of all algorithms converge with resolution  $\Delta x = L/256$ . The same problem is

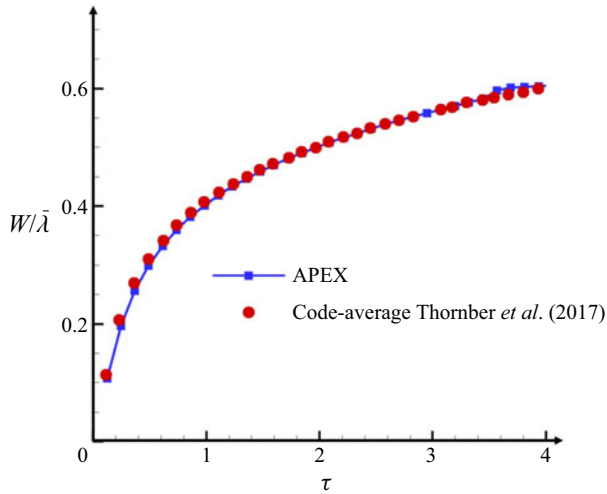


Figure 17. Comparison of the mixing-zone width with the work of Thornber *et al.* (2017).

simulated with APEX in the present work. The base resolution is  $23 \times 16 \times 16$ , on which four additional levels of refinement with a factor of 2 are applied. The finest resolution is therefore  $364 \times 256 \times 256$ . In the work of Thornber *et al.* (2017), the integral mixing width is defined as

$$W = \int_0^{L_x} \bar{Z}_1 \bar{Z}_2 dx, \tag{A1}$$

where  $\bar{Z}_{1,2}$  indicates the  $(y, z)$  plane (the spanwise directions) averaged volume fraction of species 1, 2, where species 1 is the heavy gas. The results obtained by APEX show good agreement with those of Thornber *et al.* (2017), as shown in figure 17, which proves the reliability of APEX for simulating the interfacial instability problem.

## Appendix B. Grid/computation domain convergence analysis

### B.1. Grid

The grid convergence is discussed in this subsection. All of the set-ups are summarized in tables 4 and 5. Figures 18, 19 and 20 present the results of the grid convergence test for three cases with different initial perturbations. Good grid convergence is shown between the cases G2048 and G4096 in 2-D simulations. The grid convergence is also shown between the cases G512-4 and G512-5 in 3-D simulations, which indicates that the result of the mixing width is not sensible for our finest grid set-up. Therefore, we present the numerical results of the cases G4096 and G512-5 in the present work.

### B.2. Computational domain

The fluid quantities behind the cylindrical shock wave are not uniform with radius. For the convergent geometry, at the boundaries of the  $(x, y)$  plane, the gradients of the fluid quantities are not zero. Hence if the outflow boundary condition is applied at the  $(x, y)$  plane, the perturbations at the boundaries will propagate to the interior and may influence the numerical results. Therefore, it is necessary to verify the convergence about the computation domain width to make sure that the perturbation does not propagate into the

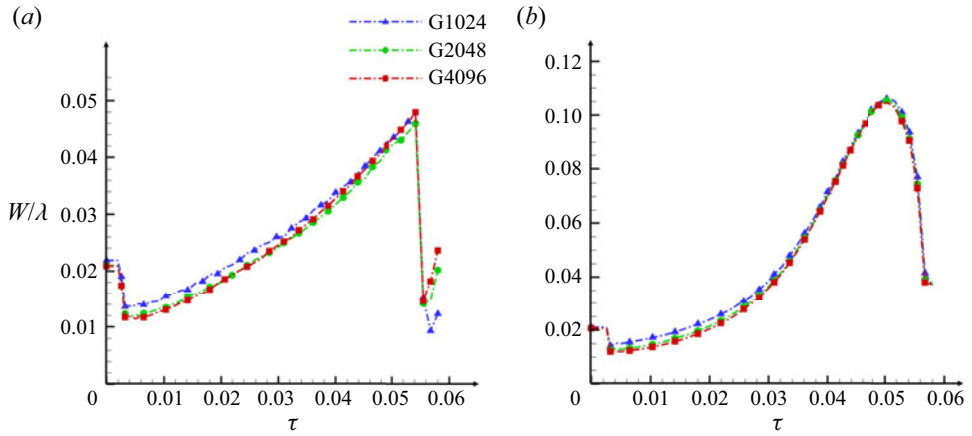


Figure 18. For the case SP8, grid convergence test for the mixing width in (a) the planar geometry and (b) the cylindrical geometry.

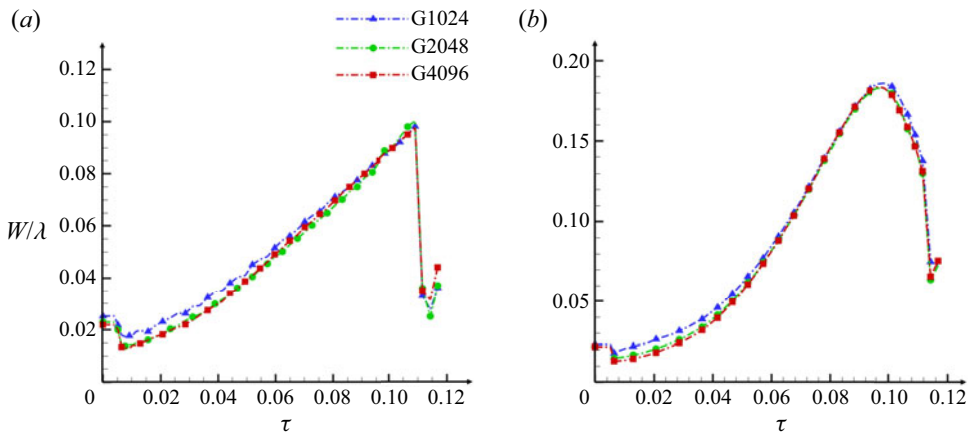


Figure 19. For the case SP16, grid convergence test for the mixing width in (a) the planar geometry and (b) the cylindrical geometry.

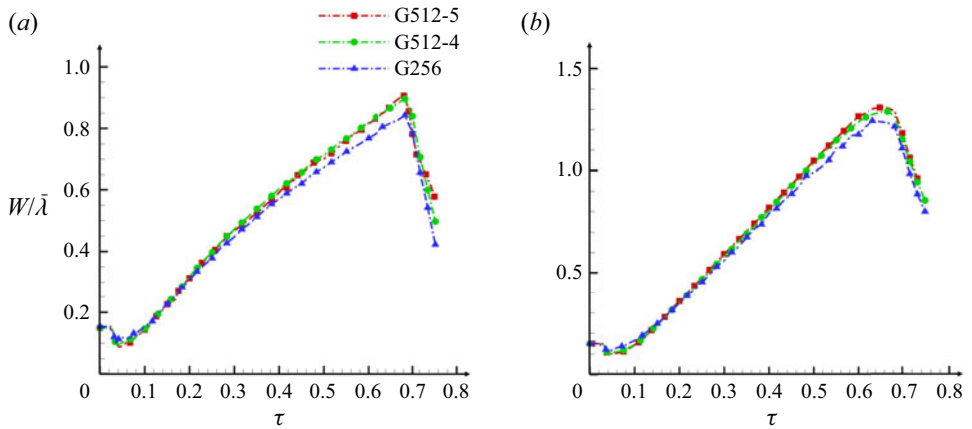


Figure 20. For the cases MP16–48, grid convergence test for the mixing width in (a) the planar geometry and (b) the cylindrical geometry.

Initial perturbation	Base resolution ( $x \times y(\times z)$ )	Case	Refinement level	$\Delta x_{min}(\times 10^{-4}R_0)$
SP8/SP16	1024 <sup>2</sup>	G1024	4	15.2
	2048 <sup>2</sup>	G2048		7.6
	4096 <sup>2</sup>	G4096		3.8
MP16-48	256 $\times$ 256 $\times$ 64	G256	4	60.8
	512 $\times$ 512 $\times$ 128	G512-4	5	30.4
	512 $\times$ 512 $\times$ 128	G512-5		15.2

Table 4. For the cylindrical cases, the grid set-ups for each case.

Initial perturbation	Base resolution ( $x \times y(\times z)$ )	Case	Refinement level	$\Delta x_{min}(\times 10^{-4}R_0)$
SP8/SP16	1024 $\times$ 256	G1024	4	15.2
	2048 $\times$ 512	G2048		7.6
	4096 $\times$ 1024	G4096		3.8
MP16-48	256 $\times$ 64 $\times$ 64	G256	4	60.8
	512 $\times$ 128 $\times$ 128	G512-4	5	30.4
	512 $\times$ 128 $\times$ 128	G512-5		15.2

Table 5. For the planar cases, the grid set-ups for each case.

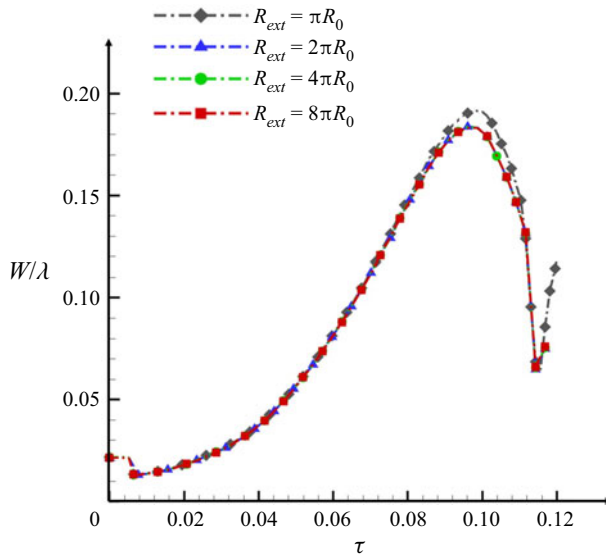


Figure 21. For the case SP16 in the cylindrical geometry, domain width convergence test for the mixing width.

zone in which we are interested. As the convergent shock wave configuration is identical in all the cylindrical cases, here we take the case SP16 as an example. Figure 21 verifies the convergence about the computation domain width. We tested domain widths  $R_{ext} = \pi R$ ,  $2\pi R$ ,  $4\pi R$  and  $8\pi R$  with the finest resolution and refinement level the same as G4096. The

results show a very good convergence. To avoid the influence of the boundary and to save computation resource at the same time, we choose  $R_{ext} = 4\pi R$  in the present work.

REFERENCES

- BARNES, C.W., *et al.* 2002 Observation of mix in a compressible plasma in a convergent cylindrical geometry. *Phys. Plasma* **9** (11), 4431–4434.
- BECK, J.B. 1996 The effects of convergent geometry on the ablative Rayleigh–Taylor instability in cylindrical implosions. PhD thesis, Purdue University.
- BELL, G.I. 1951 Taylor instability on cylinders and spheres in the small amplitude approximation. *Tech. Rep.* LA-1321. Los Alamos National Laboratory.
- BETTI, R. & HURRICANE, O.A. 2016 Inertial-confinement fusion with lasers. *Nat. Phys.* **12** (5), 435–448.
- BROUILLETTE, M. 2002 The Richtmyer–Meshkov instability. *Annu. Rev. Fluid Mech.* **34** (1), 445–468.
- CHISNELL, R.F. 1998 An analytic description of converging shock waves. *J. Fluid Mech.* **354**, 357–375.
- DIMONTE, G. 2021 A modal wave-packet model for the multi-mode Richtmyer–Meshkov instability. *Phys. Fluids* **33** (1), 014108.
- DIMONTE, G., *et al.* 2004 A comparative study of the turbulent Rayleigh–Taylor instability using high-resolution three-dimensional numerical simulations: the alpha-group collaboration. *Phys. Fluids* **16** (5), 1668–1693.
- DING, J., SI, T., YANG, J., LU, X., ZHAI, Z. & LUO, X. 2017 Measurement of a Richtmyer–Meshkov instability at an air–SF<sub>6</sub> interface in a semiannular shock tube. *Phys. Rev. Lett.* **119** (1), 014501.
- EL RAFAEI, M. & THORNER, B. 2020 Numerical study and buoyancy–drag modeling of bubble and spike distances in three-dimensional spherical implosions. *Phys. Fluids* **32** (12), 124107.
- EL RAFAEI, M., FLAIG, M., YOUNGS, D.L. & THORNER, B. 2019 Three-dimensional simulations of turbulent mixing in spherical implosions. *Phys. Fluids* **31** (11), 114101.
- EPSTEIN, R. 2004 On the Bell–Plesset effects: the effects of uniform compression and geometrical convergence on the classical Rayleigh–Taylor instability. *Phys. Plasma* **11** (11), 5114–5124.
- FLAIG, M., CLARK, D., WEBER, C., YOUNGS, D.L. & THORNER, B. 2018 Single-mode perturbation growth in an idealized spherical implosion. *J. Comput. Phys.* **371**, 801–819.
- GE, J., ZHANG, X., LI, H. & TIAN, B. 2020 Late-time turbulent mixing induced by multimode Richtmyer–Meshkov instability in cylindrical geometry. *Phys. Fluids* **32** (12), 124116.
- GONCHAROV, V.N. & LI, D. 2005 Effects of temporal density variation and convergent geometry on nonlinear bubble evolution in classical Rayleigh–Taylor instability. *Phys. Rev. E* **71** (4), 046306.
- HSING, W.W., BARNES, C.W., BECK, J.B., HOFFMAN, N.M., GALMICHE, D., RICHARD, A., EDWARDS, J., GRAHAM, P., ROTHMAN, S. & THOMAS, B. 1997 Rayleigh–Taylor instability evolution in ablatively driven cylindrical implosions. *Phys. Plasma* **4** (5), 1832–1840.
- HSING, W.W. & HOFFMAN, N.M. 1997 Measurement of feedthrough and instability growth in radiation-driven cylindrical implosions. *Phys. Rev. Lett.* **78** (20), 3876.
- JOGGERST, C.C., NELSON, A., WOODWARD, P., LOVEKIN, C., MASSER, T., FRYER, C.L., RAMAPRABHU, P., FRANCOIS, M. & ROCKEFELLER, G. 2014 Cross-code comparisons of mixing during the implosion of dense cylindrical and spherical shells. *J. Comput. Phys.* **275**, 154–173.
- LANIER, N.E., BARNES, C.W., BATHA, S.H., DAY, R.D., MAGELSSSEN, G.R., SCOTT, J.M., DUNNE, A.M., PARKER, K.W. & ROTHMAN, S.D. 2003 Multimode seeded Richtmyer–Meshkov mixing in a convergent, compressible, miscible plasma system. *Phys. Plasma* **10** (5), 1816–1821.
- LI, C.K., *et al.* 2004 Effects of nonuniform illumination on implosion asymmetry in direct-drive inertial confinement fusion. *Phys. Rev. Lett.* **92** (20), 205001.
- LI, H., HE, Z., ZHANG, Y. & TIAN, B. 2019 On the role of refraction/compression waves in Richtmyer–Meshkov instability with reshock. *Phys. Fluids* **31** (5), 054102.
- LI, H., TIAN, B., HE, Z. & ZHANG, Y. 2021 Growth mechanism of interfacial fluid-mixing width induced by successive nonlinear wave interactions. *Phys. Rev. E* **103** (5), 053109.
- LOMBARDINI, M. & PULLIN, D.I. 2009 Startup process in the Richtmyer–Meshkov instability. *Phys. Fluids* **21** (4), 044104.
- LOMBARDINI, M., PULLIN, D.I. & MEIRON, D.I. 2014a Turbulent mixing driven by spherical implosions. Part 1. Flow description and mixing-layer growth. *J. Fluid Mech.* **748**, 85–112.
- LOMBARDINI, M., PULLIN, D.I. & MEIRON, D.I. 2014b Turbulent mixing driven by spherical implosions. Part 2. Turbulence statistics. *J. Fluid Mech.* **748**, 113–142.
- LUO, X., DING, J., ZHAI, Z. & SI, T. 2018a 16th International Workshop of the Physics of Compressible Turbulent Mixing. *Tech. Rep.* Advanced Propulsion Laboratory, University of Science and Technology of China.

## Stretching/compression in convergent RM instability

- LUO, X., LI, M., DING, J., ZHAI, Z. & SI, T. 2019 Nonlinear behaviour of convergent Richtmyer–Meshkov instability. *J. Fluid Mech.* **877**, 130–141.
- LUO, X., ZHANG, F., DING, J., SI, T., YANG, J., ZHAI, Z. & WEN, C.Y. 2018b Long-term effect of Rayleigh–Taylor stabilization on converging Richtmyer–Meshkov instability. *J. Fluid Mech.* **849**, 231–244.
- MESHKOV, E.E. 1969 Instability of the interface of two gases accelerated by a shock wave. *Fluid Dyn.* **4** (5), 101–104.
- MIKAELIAN, K.O. 1990 Stability and mix in spherical geometry. *Phys. Rev. Lett.* **65** (8), 992.
- MIKAELIAN, K.O. 2005 Rayleigh–Taylor and Richtmyer–Meshkov instabilities and mixing in stratified cylindrical shells. *Phys. Fluids* **17** (9), 094105.
- PLESSET, M.S. 1954 On the stability of fluid flows with spherical symmetry. *J. Appl. Phys.* **25** (1), 96–98.
- RAYLEIGH, LORD 1882 Investigation of the character of the equilibrium of an incompressible heavy fluid of variable density. *Proc. R. Math. Soc.* **s1-14** (1), 170–177.
- RECKINGER, S.J., LIVESCU, D. & VASILYEV, O.V. 2016 Comprehensive numerical methodology for direct numerical simulations of compressible Rayleigh–Taylor instability. *J. Comput. Phys.* **313**, 181–208.
- RICHTMYER, R.D. 1960 Taylor instability in shock acceleration of compressible fluids. *Commun. Pure Appl. Maths* **13** (2), 297–319.
- SI, T., LONG, T., ZHAI, Z. & LUO, X. 2015 Experimental investigation of cylindrical converging shock waves interacting with a polygonal heavy gas cylinder. *J. Fluid Mech.* **784**, 225–251.
- SUTHERLAND, W. 1893 The viscosity of gases and molecular force. *Phil. Mag.* **36** (223), 507–531.
- TAYLOR, G.I. 1950 The instability of liquid surfaces when accelerated in a direction perpendicular to their planes. *Proc. R. Soc. Lond. A* **201** (1065), 192–196.
- THOMAS, V.A. & KARES, R.J. 2012 Drive asymmetry and the origin of turbulence in an ICF implosion. *Phys. Rev. Lett.* **109** (7), 075004.
- THORNER, B., DRIKAKIS, D., YOUNGS, D.L. & WILLIAMS, R.J.R. 2010 The influence of initial conditions on turbulent mixing due to Richtmyer–Meshkov instability. *J. Fluid Mech.* **654**, 99–139.
- THORNER, B., *et al.* 2017 Late-time growth rate, mixing, and anisotropy in the multimode narrowband Richtmyer–Meshkov instability: the  $\theta$ -group collaboration. *Phys. Fluids* **29** (10), 105107.
- TRITSCHLER, V.K., OLSON, B.J., LELE, S.K., HICKEL, S., HU, X.Y. & ADAMS, N.A. 2014 On the Richtmyer–Meshkov instability evolving from a deterministic multimode planar interface. *J. Fluid Mech.* **755**, 429–462.
- TUBBS, D.L., BARNES, C.W., BECK, J.B., HOFFMAN, N.M., OERTEL, J.A., WATT, R.G., BOEHLY, T., BRADLEY, D., JAANIMAGI, P. & KNAUER, J. 1999 Cylindrical implosion experiments using laser direct drive. *Phys. Plasma* **6** (5), 2095–2104.
- WANG, L.F., WU, J.F., GUO, H.Y., YE, W.H., LIU, J., ZHANG, W.Y. & HE, X.T. 2015 Weakly nonlinear Bell–Plesset effects for a uniformly converging cylinder. *Phys. Plasma* **22** (8), 082702.
- ZHAI, Z., ZOU, L., WU, Q. & LUO, X. 2018 Review of experimental Richtmyer–Meshkov instability in shock tube: from simple to complex. *Proc. Inst. Mech. Engrs* **232** (16), 2830–2849.
- ZHANG, J., WANG, L.F., WU, J.F., YE, W.H., ZOU, S.Y., DING, Y.K., ZHANG, W.Y. & HE, X.T. 2020 The three-dimensional weakly nonlinear Rayleigh–Taylor instability in spherical geometry. *Phys. Plasma* **27** (2), 022707.
- ZHAO, Z., WANG, P., LIU, N. & LU, X. 2020 Analytical model of nonlinear evolution of single-mode Rayleigh–Taylor instability in cylindrical geometry. *J. Fluid Mech.* **900**, A24.
- ZHOU, Y. 2017a Rayleigh–Taylor and Richtmyer–Meshkov instability induced flow, turbulence, and mixing. I. *Phys. Rep.* **720**, 1–136.
- ZHOU, Y. 2017b Rayleigh–Taylor and Richtmyer–Meshkov instability induced flow, turbulence, and mixing. II. *Phys. Rep.* **723**, 1–160.
- ZHOU, Y., *et al.* 2021 Rayleigh–Taylor and Richtmyer–Meshkov instabilities: a journey through scales. *Physica D* **423**, 132838.